University of California

Los Angeles

Jet Production in Ultra-Relativistic Polarized Proton-Proton Collisions

A dissertation submitted in partial satisfaction

of the requirements for the degree

Doctor of Philosophy in Physics

by

Dylan Thein

2005

The dissertation of Dylan Thein is approved.

Ronald J. Miech

James Rosenzweig

Huan Z. Huang, Committee Co-chair

Charles A. Whitten, Committee Co-chair

University of California, Los Angeles

2005

To Drew, Sarah, and Katie ...

My favorite-est brother and sisters ever.

Table of Contents

List of Figures

List of Tables

Acknowledgments

A great big thank you to everyone in our UCLA research group. I am particularly indebted to professors George Igo, Huan Huang, and Chuck Whitten for all of the the direction and opportunities they have provided me. A thank you to Stephen Trentalange, who taught me everything I know about experimental physics. I would also like to thank Vahe Ghazikhanian as well as all the fellow students and post-docs, whose fellowship and camaraderie was greatly appreciated.

This work would not have been possible without the STAR spin working group, a thank you to all those I've worked with including but not limited to: Akio Ogawa, Les Bland, Steve Vigdor, Joanna Kiryluk, Ernst Sichtermann, Rene Fatemi, Mike Miller, and Thomas Henry. Addtionally thank you to all those who worked and contributed to the the Barrel EMC sub-system, particularly Alex Suaide, Marcia de Moura, Alex Stolpovsky, and Oleg Tsai.

Last but not least I would like to give a special thank you to my family and friends. Although none of you actually contributed to this thesis (despite my pleas), your support, understanding, and laughter kept me going long enough to complete it, and for that I am grateful.

Vita

1978	Born, Iowa City, Iowa, USA.
2000	B.S. (Physics) and B.S. (Mathematics), Creighton University.
2000–2001	Teaching Assistant, Physics Department, UCLA. Led discussions of Physics 124 (Nuclear Physics Lecture) under direction of George Igo. Led discussions of Physics 10 (Concepts of Physics) under direction of Kusenko. Led discussions of Physics 6A (Introductory Physics) under direction of Chetan Nayak.
2003	M.S. (Physics), UCLA, Los Angeles, California.
2001–present	Research Assistant, Physics Department, UCLA.

Publications

J. Adams *et al.*

Multiplicity and Pseudorapadity Distributions of Photons in Au+Au Collisions at $\sqrt{s_{_{NN}}} = 62.4$ GeV *Phys. Rev. Lett.* **95**:062301, 2005.

J. Adams *et al.*

Pion Interferometry in Au+Au Collisions at $\sqrt{s_{_{NN}}} = 200$ GeV. *Phys. Rev.* **C71**:044906, 2005.

J. Adams *et al.*

Pseudorapidity Asymmetry and Centrality Dependence of Charged Hadron Spectra in d+Au Collisions at $\sqrt{s_{NN}} = 200$ GeV. *Phys. Rev.* **C70**:064907, 2004.

J. Adams *et al.*

Open Charm Yields in d+Au Collisions at $\sqrt{s_{NN}} = 200$ GeV. *Phys. Rev. Lett.* **94**:062301, 2005.

J. Adams *et al.*

Measurements of Transverse Energy Distributions in Au+Au Collisions at $\sqrt{s_{NN}} =$ 200 GeV. *Phys. Rev.* **C70**:054907, 2004.

J. Adams *et al.*

Transverse Momentum Dependent Modification of Dynamic Texture in Central Au+Au Collisions at $\sqrt{s_{NN}} = 200$ GeV. *Phys. Rev.* **C71**:031901, 2005.

J. Adams *et al.*

Phi Meson Production in Au+Au and p+p Collisions at $\sqrt{s_{NN}} = 200$ GeV. *Phys. Lett.* **B612**:181-189, 2005.

J. Adams *et al.*

Centrality and Psuedorapidity Dependence of Charged Hardron Production at Intermediate pT in Au+Au Collisions at $\sqrt{s_{NN}} = 200$ GeV. *Phys. Rev.* **C70**:044901, 2004.

J. Adams *et al.*

Three Pion HBT Correlations in RHIC Collisions from the STAR Experiment *Phys. Rev. Lett.* **91**:262301, 2003.

J. Adams *et al.*

Experimental and Theoretical Challenges in the Search for the Quark Gluon Plasma: The STAR Collaboration's Critical Assessment of the Evidence from RHIC Collisions. *Nucl. Phys.* **A757**:102-183, 2005.

J. Adams *et al.*

K(892) Resonance Production in Au+Au and p+p Collisions at $\sqrt{s_{NN}} = 200$ GeV at STAR. *Phys. Rev.* **C71**:064902, 2005.

J. Adams *et al.*

Production of e+e- Pairs Accompanied by Nuclear Dissociation in Ultra-Peripheral Heavy Ion Collisions. *Phys. Rev.* **C70**:031902, 2004.

J. Adams *et al.*

Photon and Neutral Pion Production in Au+Au Collisions at $\sqrt{s_{NN}} = 130$ GeV. *Phys. Rev.* **C70**:044902, 2004.

J. Adams *et al.*

Azimuthally Sensitive HBT in Au+Au Collisions at $\sqrt{s_{NN}} = 200$ GeV. *Phys. Rev. Lett.* **93**:012301, 2004.

J. Adams *et al.*

Cross sections and Transverse Single Spin Asymmetries in Forward Neutral Pion

Production from Proton Collisions at $\sqrt{s_{NN}}$ = 200 GeV. *Phys. Rev. Lett.* **92**:171801, 2004.

J. Adams *et al.*

Azimuthal Anisotropy at RHIC:The First and Fourth Harmonics. *Phys. Rev. Lett.* **92**:062301, 2004.

J. Adams *et al.*

Identified Particle Distrubutions in p+p and Au+Au Collisions at $\sqrt{s_{NN}}$ = 200 GeV. *Phys. Rev. Lett.* **92**:112301, 2004.

J. Adams *et al.*

Pion, Kaon, Proton and Anti-Proton Transvserse Momentum Distributions from p+p and d+Au Collisions at $\sqrt{s_{NN}}$ = 200 GeV. *Phys. Lett.* **B6**:8-16, 2005.

J. Adams *et al.*

Event by Event Mean pT Fluctations in Au-Au Collisions at $\sqrt{s_{NN}}$ = 130 GeV. *Phys. Rev.* **C71**:064906, 2005.

J. Adams *et al.*

Pion Kaon Correlations in Au-Au Collisions at $\sqrt{s_{NN}}$ = 130 GeV. *Phys. Rev. Lett.* **91**:262302, 2003.

J. Adams *et al.*

Multistrange Baryon Production in Au+Au Collisions at $\sqrt{s_{NN}}$ = 130 GeV. *Phys. Rev. Lett.* **92**:182301, 2004.

J. Adams *et al.*

Rho0 Production and Possible Modification in Au+Au and p+p Collisions at $\sqrt{s_{NN}}$ = 200 GeV. *Phys. Rev. Lett.* **92**:092301, 2004.

J. Adams *et al.*

Multiplicity Fluctations in Au+Au Collisions at $\sqrt{s_{NN}}$ = 130 GeV. *Phys. Rev.* **C68**:044905, 2003.

J. Adams *et al.*

Rapidity and Centrality Dependence of Proton and Anit-Proton Production from Au+Au Collisions at $\sqrt{s_{NN}}$ = 200 GeV. *Phys. Rev.* **C70**:041901, 2004.

J. Adams *et al.*

Evidence from d+Au Measurements for Final State Suppression of High pT Hadrons in Au+Au Collisions at RHIC. *Phys. Rev. Lett.* **91**:072304, 2003.

J. Adams *et al.*

Particle Type Dependence of Azimuthal Anisotropy and Nuclear Modification of Particle Production in Au+Au Collisions at $\sqrt{s_{NN}}$ = 200 GeV. *Phys. Rev. Lett.* **92**:052302, 2004.

Abstract of the Dissertation

Jet Production in Ultra-Relativistic Polarized Proton-Proton Collisions

by

Dylan Thein

Doctor of Philosophy in Physics

University of California, Los Angeles, 2005

Professor Charles A. Whitten, Co-chair

Professor Huan Z. Huang, Co-chair

Understanding the nucleon's spin structure is of great interest to fundamental science. Well aware that quarks, gluons and anti-quarks comprise the nucleon, the scientific community expectation was that the the three valence quarks would carry most of the nucleon's spin. However in 1987 the EMC experiment, looking at deep-inelastic scattering, noted that the quarks and anti-quarks could contribute no more than a third to the proton's total spin. This meant that gluons and/or angular momentum must account for the remainder of and majority of the nucleon's spin.

The physics community has now turned to a concerted exploration of the gluon sector with much of the effort concentrated at RHIC. RHIC is the first collider to provide polarized proton on proton collisions. Currently running at $\sqrt{s}$=200 GeV and capable of obtaining $\sqrt{s}$=500 GeV, RHIC and the detectors associated with it, notably STAR and PHENIX, can probe these low x region of the nucleon where a substantial gluon contribution to the total spin could exist.

Measuring the gluon spin contribution to the nucleon, ΔG, and thereby determining the possible existence and magnitude of an associated orbital momentum, is the highest near term goal of STAR's spin group. In principle several measurement are possible involving the hard scattering of gluons that should give us insight into ΔG. Currently the channel most accessible to STAR is that of inclusive jets. By comparing the cross section of the jets with respect to the protons spin orientations, we can form the longitudinal double spin asymmetry, A_{LL}, which is expected to be sensitive to the gluon's polarization. In the following years, when RHIC luminosity permits, the cleaner di-jet and γ-jet channels may be analysed to pin down ΔG as a function of x.

Typically jets derive from three leader order processes: qq, qg and gg. Jets produced with transverse momentums ranging from 5-15 GeV are most likely to be products of gg or qg reactions, each reaction contributing to the measured asymmetry. This asymmetry must then be extrapolated into a gluon polarization using one of several pQCD models. Here the energy range and inclusiveness of the measurement become problematic. pQCD mandates high energies if one wants precision; most of our data is in the intermediate P_T region where the accuracy of the approximations are not well known. Further, by not selecting out a single channel, processes such as qq contaminate the measurement. To understand the measurement one needs to understand not only how much of the signal is contamination, but also how much of the signal comes from gg interactions and how much from qg interactions, all the while keeping in mind the biases induced by the trigger. That said, inclusive jets are an excellent start to what will provide the best understanding of ΔG to date.

CHAPTER 1

Introduction

The nuclear physics community is actively engaged in a program seeking to measure the internal structure of the nucleon. Theory is unable to predict these quantities from first principle, therefore we must determine their values through experimental means. Several aspects of the nucleon's structure are now well established thanks to a series of deep inelastic scattering (DIS) and polarized deep inelastic scattering (pDIS) experiments occurring over the past thirty years.

The next important step along these lines is to understand the gluon's contribution to the proton's spin. Particular interest in this quantity exists due to previous results from pDIS experiments. Counter to expectations, the pDIS experiments showed and later verified that the bulk of the nucleon's spin is not held by the nucleon's quarks [Ash88].

By colliding polarized protons with one another at relativistic energies, detectors at RHIC will provide the most definitive measurement of the gluon polarization worldwide [Aid05]. Combined with existing knowledge of the proton's total spin as well as the quark's contribution to this total, knowledge of the gluon polarization will determine if the proton's constituents carry orbital angular momentum, i.e. net motion around the proton's center.

The RHIC spin program is only now leaving its infancy and several years are necessary before RHIC is operating at full capacity. This thesis provides

the initial results - including the jet production asymmetry, a quantity sensitive to the gluon polarization - from the STAR detector. Although the results presented will prove statistically limited, they outline the program's future as well as documenting its progress.

1.1 Historical Background

The concept of spin dates back to celestial mechanics, when bodies where observed to rotate about themselves (in rotation) and other bodies (in revolution). These ideas persist in modern quantum mechanics, with one notable difference. The self-rotation, or spin, of an object is no longer associated with physical motion, but instead it is an intrinsic quality found in all known elementary particles.

In 1922 Stern and Gerlach first observed this quantum nature of spin by passing silver atoms through a heterogeneous magnetic field [Est33]. This experiment, although itself inconclusive, led to the discovery that electrons carry a spin of $\frac{1}{2}$, and when placed in a magnetic field the electron's spin would always align or anti-align with the field's direction. A decade later Stern more precisely repeated the experiment with protons and dueterons instead of silver atoms. The measurement of the proton's magnetic moment confirmed the half-integer quantum nature seen in the electron's spin also existed in the proton.

Today it is well known that the proton, like the neutron, is a composite object, made up of quarks, gluons, and anti-quarks. Together, these particles, collectively known as the nucleon's *partons*, can be described as an interacting soup, with new particles and their corresponding anti-particle pairs coming into and out of existence through the vacuum.

The partons all carry a portion of the proton's total spin, and may do so

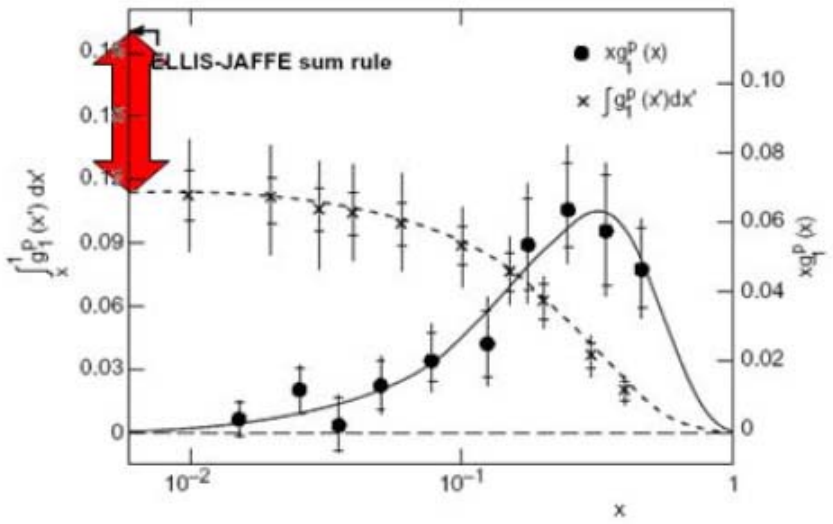

Figure 1.1: The EMC's original findings are inconsistent with the expectations of Ellis-Jaffe sum rule. g_1 is the charge weighted sum of the quark's spin distribution functions; $g(x)_1 = \sum e_i^2 \Delta f(x)_i$.

in two ways: through the particle's intrinsic spin, or through it's orbital angular momentum - orbital angular momentum is a collective motion about the proton's center, much like earth's revolving around the sun. We would like to verify that the summed spins of these pieces are reconcilable with the total observed spin of the proton, as well as understand the contribution from any given piece in a meaningful way.

Experiments performed at SLAC attempted to disentangle the proton's spin by colliding polarized electrons on a polarized proton target, becoming the first in a line of polarized Deep Inelastic Scattering (pDIS) experiments. The European Muon Collaboration (EMC) continued this work in the mid 1980's with the goal of measuring the quark and anti-quark's contribution to the proton's spin, and the results at the time were surprising.

As mentioned above, the proton and neutron are composite and dynamic objects, however they are commonly labeled by their three static pieces, the valence quarks. The valence quarks were expected to account for most of if not all of the nucleon's spin. Instead, the measurement showed the total quark contribution to the nucleon's spin was nearer 20% [Ash88]. This result was dubbed "the spin crisis" and generated a great deal of activity within the physics comunity.

1.2 The Components of the Nucleon's Spin

The nucleon's spin may be described by the simple sum

$$\frac{1}{2} = \frac{1}{2}\Delta Q + \Delta G + < L_z > \tag{1.1}$$

Here the left hand side of the equation is the proton's spin and ΔQ and ΔG are the average number of quarks and gluons aligned in the direction of the proton's spin. The factor of $\frac{1}{2}$ preceding ΔQ accounts for the quarks intrinsic half-integer spin, whereas gluons carry a full unit of spin. Lastly, L_z is the combined angular momentum of the quarks and gluons.

Figure 1.2 summarizes the understanding of the nucleon's spin distribution functions to date. The predictions given are valid at the particular Q^2 value of 1 GeV, where $Q^2 = -q^2$ and q is the relativistic momentum transfer between scattered particles.

The spin structure functions are plotted against the variable Bjorken x, which may be described as the fraction of the proton's momentum carried by the quark or gluon.

$$x = \frac{p_i}{p_{proton}}, \qquad \sum p_i = p_{proton} \tag{1.2}$$

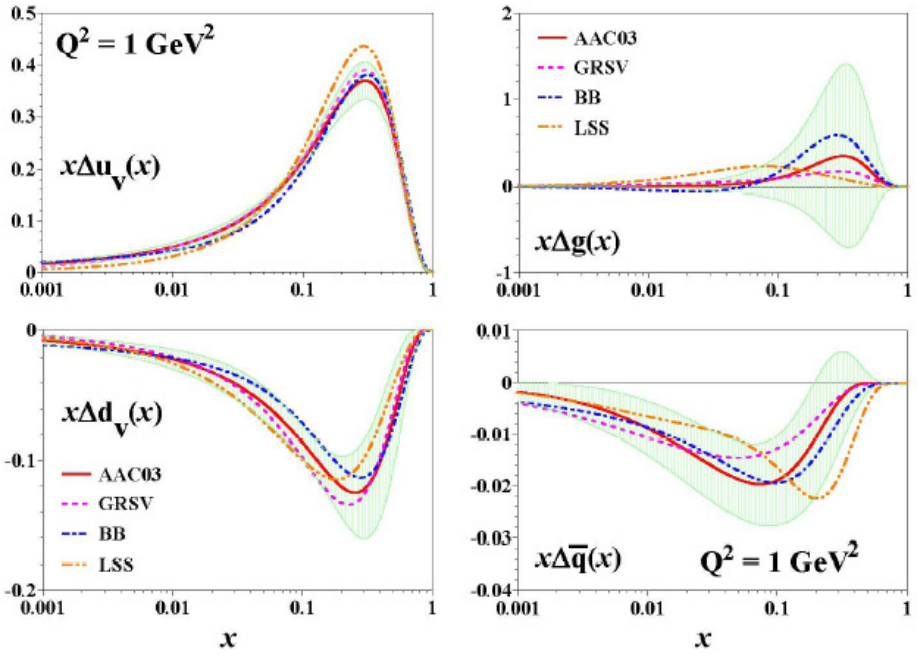

Figure 1.2: Data taken from all polarized DIS experiments is fit by competing phenomenological models, and used to extrapolate the spin distribution functions of the quarks and gluons. The relatively well understood up and down valence quark distributions are drawn on the left. Anti-quarks are depicted in the bottom right-hand corner, and the gluon distribution is plotted in above on the right. The shaded region represents the error bars associated with the Asymmetry Analysis Collaboration (AAC03) [Har03]. As indicated by the figure, the gluon polarization is poorly constrained in both magnitude and sign. The STAR and PHENIX detectors will measure several channels sensitive to the gluon's polarization over the next few years, helping to better constrain this quantity

We may determine the quantities $< \Delta Q >$ and $< \Delta G >$ from their associated spin distribution functions by integrating over all x at a given value of Q^2.

$$\Delta Q = \int \Delta q(x_F)\ d(x_F) \Big|_{Q^2}$$
$$\Delta G = \int \Delta g(x_F)\ d(x_F) \Big|_{Q^2} \tag{1.3}$$

A global analysis carried out by the Asymmetry Analysis Collaboration (AAC) in 2003 using results from SLAC experiments and HERMES reports ΔQ to be 0.213 ± 0.138 [Har03]. One analysis of the SMC data reports this quantity to be $0.19 \pm 0.05(\text{stat}) \pm 0.04(\text{syst})$[Ade98]. The different measurements are taken at different Q^2 and are therefore not expected to be identical. However they are statistically consistent with one another.

With $\Delta q(x)$ relatively well understood by polarized DIS, the next step necessary to understand the spin structure of the nucleon is to measure the gluon contribution, the integral ΔG. The AAC's analysis currently places somewhat large limits on ΔG, quoting 0.5 ± 1.27 [Har03].

Final results from STAR are strongly dependent on future running conditions. If no debilitating problems are faced, STAR hopes to narrow the bounds on ΔG to within $\pm$ 0.5. The exclusive channel, jet+γ, is expected to be the primary experimental forus that will allow STAR to improve on past results.

As experiments mature we may begin to examine the gluon structure function, $\Delta g(x)$, giving us a more detailed understanding of the nucleon structure. Several experiments are participating in this effort, including COMPASS at CERN lab, HERA at DESY, and the PHENIX and STAR detectors located at Brookhaven National Lab (BNL).

1.3 ΔG at STAR

The gluon polarization is accessible through many physical processes, and is certainly not limited to polarized DIS experiments. RHIC is expected to dominate this measurement in the upcoming years through its polarized proton-proton collision program. Specifics of the RHIC program will be developed in the following chapter. For now it is sufficient to state that RHIC is capable of providing longitudinally polarized proton collisions at sufficiently high energies to begin the study of the gluon polarization.

Within the RHIC program and specifically at the STAR detector, several physical processes sensitive to the gluon polarization are accessible for study. These include inclusive jet production, $pp \rightarrow$ jet+X, di-jet production, $pp \rightarrow$ jet+jet=X, heavy flavor production, $pp \rightarrow (Q\bar{Q})$X, and direct photon plus jet production, $pp \rightarrow \gamma$+jet+X.

Each process possesses inherit advantages, and is likewise limited in other respects. The cleanest channels, such as $pp \rightarrow (Q\bar{Q})$X and $pp \rightarrow \gamma$+jet, are the rarest due to their small cross-sections. Particularly high hopes rest in observing direct photons and jets. This is because the channel's gluon-sensitive signal, the Compton subprocess $Gq \rightarrow \gamma$+jet, is expected to dominate over its background, the quark-antiquark annihilation subprocess $q\bar{q} \rightarrow \gamma$+jet, thereby minimizing contamination. Direct photons will provide the critical information necessary to decompose the measurement of ΔG into $\Delta G(x)$.

In order to observe a statistically meaningful sample of these rarer events, RHIC must produce a tremendous number of proton collisions. This may be accomplished by running collisions for greatly extended periods of time, or by increasing the rate of collisions through enhanced *luminosities*. Luminosity is

defined as

$$\mathcal{L} = fn\frac{N_1 N_2}{A_{overlap}} \tag{1.4}$$

Here f is the frequency of beam rotation, n is the number of bunches in the beam, N is the number of protons is a bunch, and A is the overlap area at the interaction point. Financial constraints moderate the experiment's duration from year to year in a consistent manner, so the greatest gains toward observing rare channels will come from increases to beam luminosities.

In time STAR expects to pursue all available avenues, however inclusive jet production, which has the largest cross-section of the aforementioned channels, is the most viable option at RHIC's current luminosities.

1.4 Perturbative Quantum Chromodynamics

Our best understanding of nuclear interaction, known as the strong force, derives from the theory of quantum chromodynamics (QCD). QCD is a based off the very successful theory of quantum electrodynamics (QED).

QED is the first theory to unify two of the four fundamental forces, electromagnetism and the weak force, forming the electro-weak force. Obtaining a grand-unified theory of all four fundamental forces (electro-weak, strong, and gravity) is considered by many to be the highest goal achievable by the physics community.

Precision experiments, such as the g-2 experiment located at Brookhaven Lab, agree with QED predictions to impressive degrees. The predictive power of QED relies upon perturbation theory to approximately solve the QED Lagrangian,

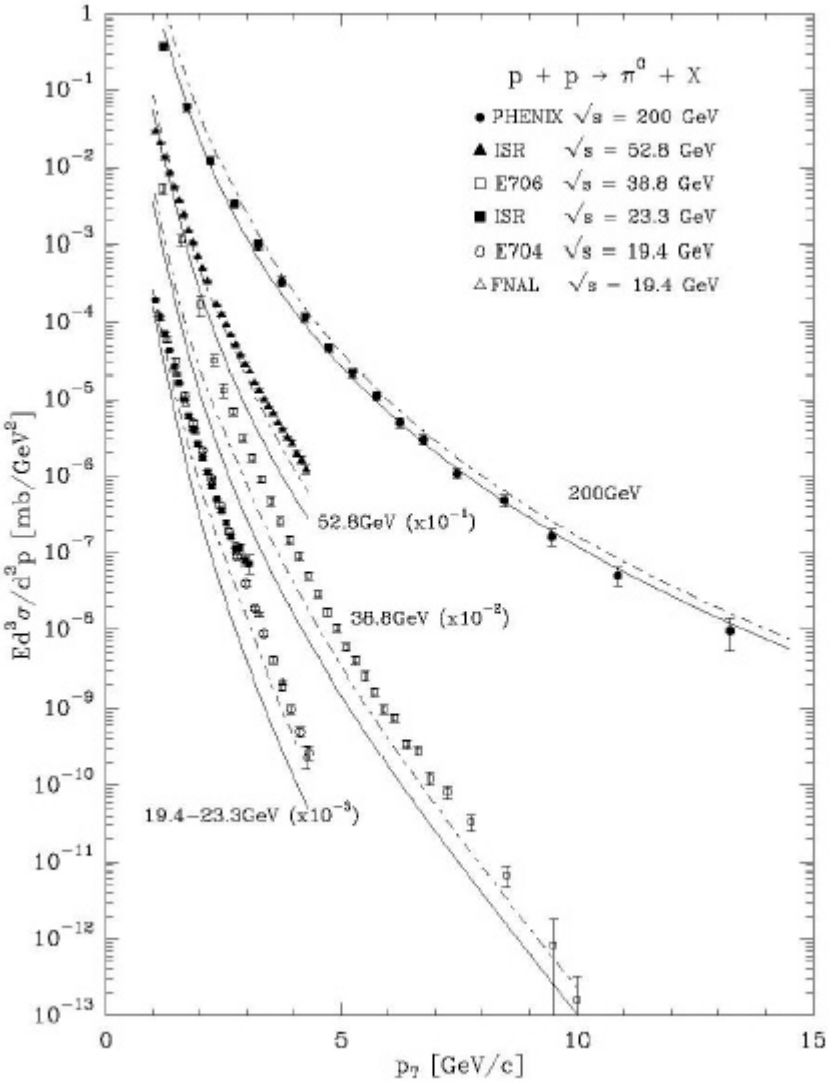

Figure 1.3: QCD has systematically under-predicted π_0 production in lower energy $p+p$ collisions [Bou03]. Recent 200 GeV results from the PHENIX detector at RHIC agree surprisingly well with next-to-leading-order (NLO) calculations.

and is accurate because the expansion variable, $\alpha = \frac{1}{137}$, is much less than 1. By calculating enough Feynam diagrams of increasing complexity, a value can be predicted to an arbitrarily good precision.

In QCD, each quark is assigned a color charge analogous to the electrical charge, and it is through this color charge that the strong interaction is governed. The gluon mediates the color charge much like the photon mediates the electromagnetic charge of QED. However, unlike the photon, the gluon is also a charge carrier, and can therefore interact directly with other gluons. This gluon-gluon interaction creates a screening, which effectively increases the magnitude of the strong force's coupling constant, α_s, precluding most perturbative calculations.

Fortunately α_s is dependent upon the momentum exchanged between particles, Q^2. That is, the more energetic the interaction, the less effective the gluon screening, and the more accurate the perturbative calculation will be. The precise value of Q^2 and p at which perturbative QCD (pQCD) becomes valid is unknown. However recent results such as the neutral pion cross-sections shown in Figure 1.3 provide much optimism for the intermediate-energy jet program at STAR. Crossing the Q^2 threshold into a region where pQCD is a viable approximation of the QCD Lagrangian is necessary in order to understand any experimental results.

The screening process may be characterized by the Dokshitzer, Gribov, Lipatov, Altarelli, and Parisi (DGLAP) equations to evolve the structure functions across a wide range of Q^2 values. Thus we can compare calculations to the results of various experiments performed at different energies. This effectively provides a lever arm which is used to better determine the distribution functions of the nucleon. Figure 1.4 depicts our current understanding of $g_1(x, Q^2)$. We hope to make a comparable picture for Δg in the upcoming years principally with data

recorded at RHIC.

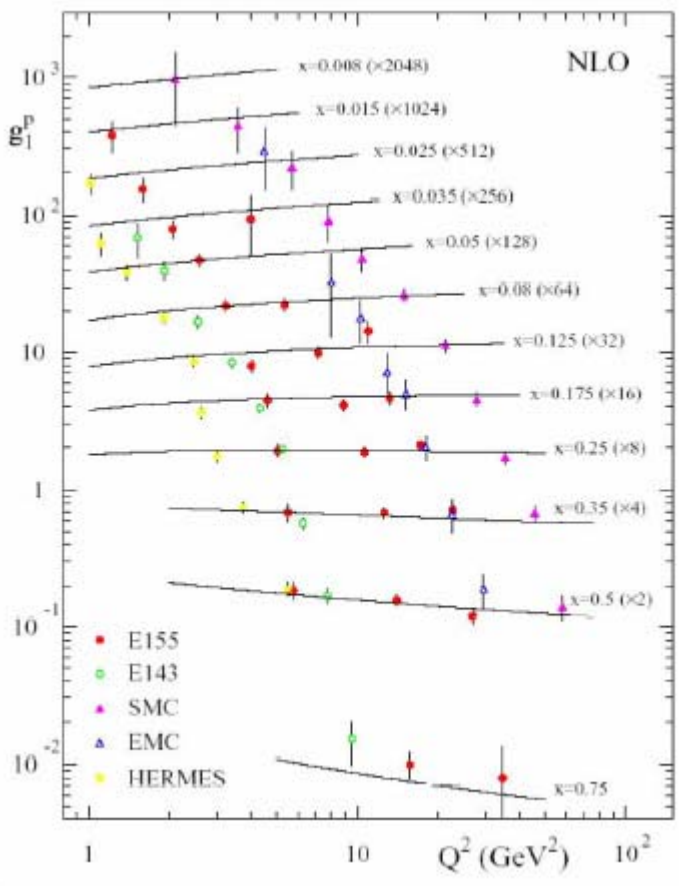

Figure 1.4: Understanding of g_1 as a function of Q^2 from polarized DIS experiments [PDG].

1.5 Jets

When a hard scattering occurs between the quarks and gluons of two nucleons the interaction may be described in two principle steps. The first step is the initial scattering of the partons. In the initial scattering the incoming and outgoing momenta of the partons are examined with the tools available from pQCD on a diagram by diagram basis. Ideally we would like to then measure the outbound

parton, however to date, a bare parton has never been observed. Instead a second step occurs prior to measurement. After the initial scattering, the outbound parton immediately *fragments* into multiple, final-state particles.

The collective group of fragmented particles resulting from a hard scattering is called a jet. We can attempt to identify a jets by grouping the final-state particles found within a localized region. Several jet reconstruction algorithms exist to preform this task, and thankfully over the past 20 years preceding experiments have taken great efforts to maximize their effectiveness.

Through jet reconstruction can we gain insight toward the outgoing momentum of the scattered parton, enabling us to directly compare our measurements with pQCD predictions.

The added complexity arising from parton fragmentation creates several experimental difficulties that must be systematically accounted for in order to understand our measurement. These will be introduced and examined in the analysis chapter of the thesis.

1.6 Production Asymmetries

A particle's spin axis necessarily breaks a physical symmetry. Because of this, a common technique used to observe spin effects is to look for asymmetries occurring in various cross-sections.

At the RHIC ring, it is convenient to redefine the three principle axes (x,y,z) into the transverse, normal and longitudinal directions (T,N,L). The L axis points in the direction of the particle's motion, the T axis points upward to the sky, and the N axis points inward toward the ring's center.

The direction of polarization is coupled to a corresponding asymmetry. In

the case of a polarized beam colliding with an unpolarized target, the three measurable asymmetries are A_T, A_N, and A_L. When a polarized beam collides with another polarized beam (or target), nine asymmetries may be examined (A_{TT}, A_{TN}, A_{TL}, ...) in addition to the original three.

At the time of collision, the proton beams at RHIC are polarized in the longitudinal direction. This facilitates the study of two asymmetries: the single-spin longitudinal asymmetry, A_L, and the double-spin longitudinal asymmetry, A_{LL}. The parity-violating asymmetry A_L may be measured in both RHIC's yellow and blue rings, and is defined by

$$A_L = \frac{1}{P}\frac{\sigma_+ - \sigma_-}{\sigma_+ + \sigma_-} \tag{1.5}$$

The magnitude of the observed beam's polarization is denoted by P and direction is denoted by (+,-). A plus refers to a positive helicity state, spin aligned with motion, and minus refers to a negative helicity state, spin anti-aligned with motion. Dependencies to $x_{Bjorken}$ Q^2 are suppressed in the cross-section's notation, σ.

Of much greater interest is the double-spin asymmetry, A_{LL}. A_{LL} is not bound by the parity conservation of the strong interaction which effectively zeroes the single-spin asymmetry A_L. Instead A_{LL} is both sensitive to the gluon's polarization and potentially large. The measurable asymmetry is defined in a similar manner as A_L

$$A_{LL} = \frac{1}{P_y P_b}\frac{(\sigma_{++} + \sigma_{--}) - (\sigma_{+-} + \sigma_{-+})}{(\sigma_{++} + \sigma_{--}) + (\sigma_{+-} + \sigma_{+-})} \tag{1.6}$$

A_{LL} compares the particle or jet production of like helicity states to that of unlike helicity states. As expected from a double-spin asymmetry, A_{LL} depends

upon the polarizations and helicities of both the yellow and blue beams. Of course physical properties of the nucleon do not depend on beam polarizations. The physical asymmetry that would be produced with a perfectly polarized beam is denoted by ϵ, and related to our measurable asymmetries as defined below

$$\begin{aligned} \epsilon_L &= P \cdot A_L \\ \epsilon_{LL} &= P_Y P_B \cdot A_{LL} \end{aligned} \tag{1.7}$$

1.7 Theoretical Expectations for A_{LL}

Because the proton is almost exclusively composed of quarks and gluons, there is little surprise that the predominant mechanisms of jet production are the three LO pQCD diagrams: qq $\rightarrow$ jet+X, qG $\rightarrow$ jet+X and GG $\rightarrow$ jet+X. These are depicted in figure 1.5. Following the LO contributors, the NLO daughter-diagrams give important corrections to jet cross-sections, particularly in the lower energy ranges where α_s is large.

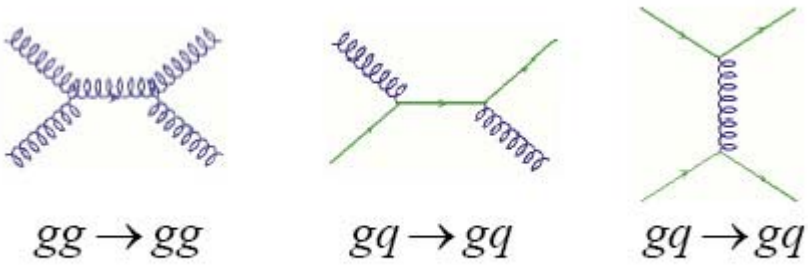

Figure 1.5: The three leading order pQCD processes that contribute to jet production: gluon-gluon, quark-gluon, and quark-quark.

When measuring a jet, the techniques available to distinguish which sub-process created the jet in question are minimal at best. This is particularly true for the low-energy jets at the focus of this analysis. Since there is no clear way to determine the origin of a jet, we must instead make an inclusive measurement, and treat all jets as equals. The task is then pushed to simulations and theory to entwine and entangle all LO and NLO sub-processes into one ensemble quantity which may be used to compare with experimental results.

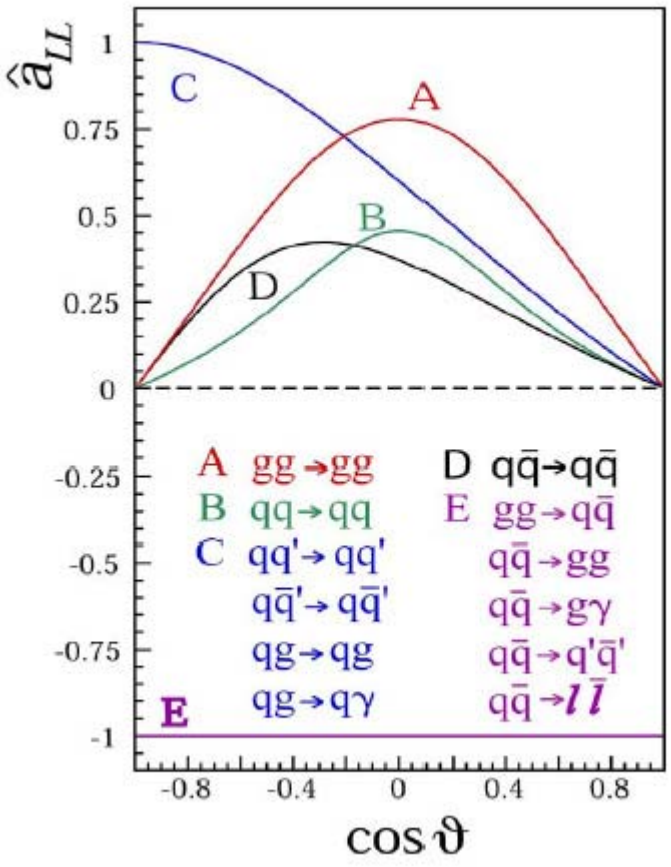

Figure 1.6: pQCD predicts explicit production asymmetries for the quark and gluon sub-processes.

The steps necessary to make predictions for an inclusive asymmetry may be categorized in three stand-alone pieces. Here is an overview of the entire process. First the sub-process's asymmetry, a_{LL}, must be determined for each diagram. It is these a_{LL}'s that will later be convoluted to form the single measurement A_{LL}. Second, fits to data from DIS experiments are used to determine the polarization distribution functions (these are the same fits from figure 1.2); the polarization distribution functions provide the weighting factors for the a_{LL}'s. Finally a statistical model is needed to predict the likelihood that a sub-process creates the jet. When all pieces are in place we may input various gluon polarization distribution functions, $\Delta G(x)$'s, and output resultant A_{LL}'s.

To obtain expectations of the sub-process' a_{LL}, pQCD calculations are used to make clear predictions of the jet's cross-sections on a diagram-by-diagram basis. By directly applying equation 1.6 we can produce an a_{LL} for each sub-process. Figure 1.6 shows the calculated asymmetries for leading order diagrams, all shown as a function of outbound jet direction $\cos\theta$.

Measurement made at the STAR detector will focus on asymmetries located between $\cos\theta = 0$ and $\cos\theta = 0.76$. Although θ is a conceptually easy variable to visualize, it does is not convienent when applying relativistic transformations. Instead we use the more appropriate variable of pseudo-rapidity, η, which is defined as

$$\eta = -\log\tan\frac{\theta}{2} \tag{1.8}$$

The range of $\cos\theta$ at STAR of $0 - 0.76$ is identical to an η range of $0 - 1$.

With the diagrams asymmetries in hand, we once again turn to pQCD calculations to establish the relationships governing the mechanisms of jet production.

These relationships are the key to convoluting the individual jet mechanisms into an ensemble cross-section thus asymmetries. Figure 1.7 plots the three mechanisms across the $p_\perp$ range of interest for this analysis. At lower values of $p_\perp$, a jet is most likely to occur from a gluon-gluon or quark-gluon scattering. As jet energies increase, contributions from gluon-gluon scatterings decline, falling in the wake of the rising quark-quark jet mechanism. However, not until transverse jet energies exceed 30 GeV does the quark-quark jet production surpass that of the quark-gluon.

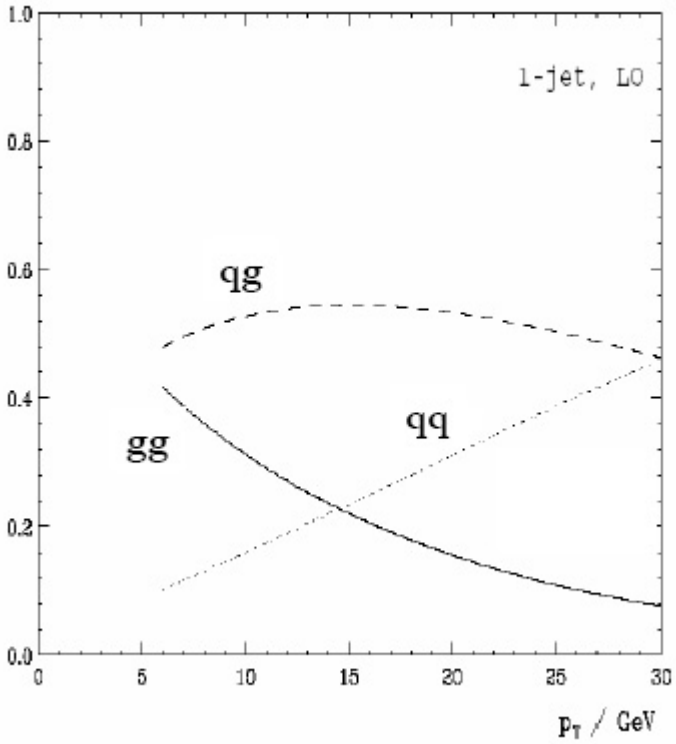

Figure 1.7: Jets form from hard scatterings of partons. The three primary contributions are quark-quark, quark-gluon, and gluon-gluon scattering. Lower energy jets are more likely to be formed from gluon-gluon scatterings. At larger jet energies, quark-quark scatterings, which are not sensitive to the gluon's polarization, are a more predominant production mechanism.

The variable $p_\perp$ is employed many times throughout this text. Often in plots

$p_\perp$ serves as the independent variable that other quantities are plotted against, consequently it is important that the reader understand precisely what the $p_\perp$ signifies and its importance. Geometrically $p_\perp$ is the simply the portion of momentum pointed perpendicular to the beam-line. Otherwise stated, it is the radial component of the vector in cylindrical coordinates.

$p_\perp$ may also be related to the initial conditions of the scattered quark or gluon, specifically through the variable of Bjorken x. Therefore $p_\perp$ serves as an important stepping stone between theory and measurement.

$$p_\perp = 2x\sqrt{s} \cdot \tan\theta \tag{1.9}$$

In the above equation, $\sqrt{s}$ is the center of mass energy of the collision, in this case 200 GeV, and Bjorken x is the momentum fraction carried by the scattered quark or gluon.

The final step is to input the polarized parton distribution functions of the proton, $q_u(x), \bar{q}_u(x)$, $q_d(x)$, $\bar{q}_d(x)$, q_s, $\bar{q}_s(x)$, and g_{x_F}. Unfortunately pQCD is unable to determine these functions from first principle, instead phenomenological models, parameterized by existing data, are used to provide the these values. Although several models exist to describe the gluon polarization, we will focus on the results from a global analysis of the pDIS data given by Gluck, Reya, Stratman and Vogelsang (GRSV).

The DIS data places strong restraints on the quark's polarizations, but only loose constraints occurring from scaling violations on the gluon's polarization. Therefore the principle unknown is the gluon's polarization. Possible gluon distributions from the GRSV model are input into the calculation and yield the final asymmetries. Conceivably $G(x)$ can be a multitude of functions, nonethe-

less because of the large uncertainties associated with the measurement in its early stages, we need only to consider a handful of scenario's for $G(x)$. Three outcomes arising from distinctly different initial conditions are shown in figure 1.8. The three inputs are the expected gluon polarization, the maximum gluon polarization, and a negative gluon polarization. The expected results vary in both magnitude and shape across the range of $p_\perp$.

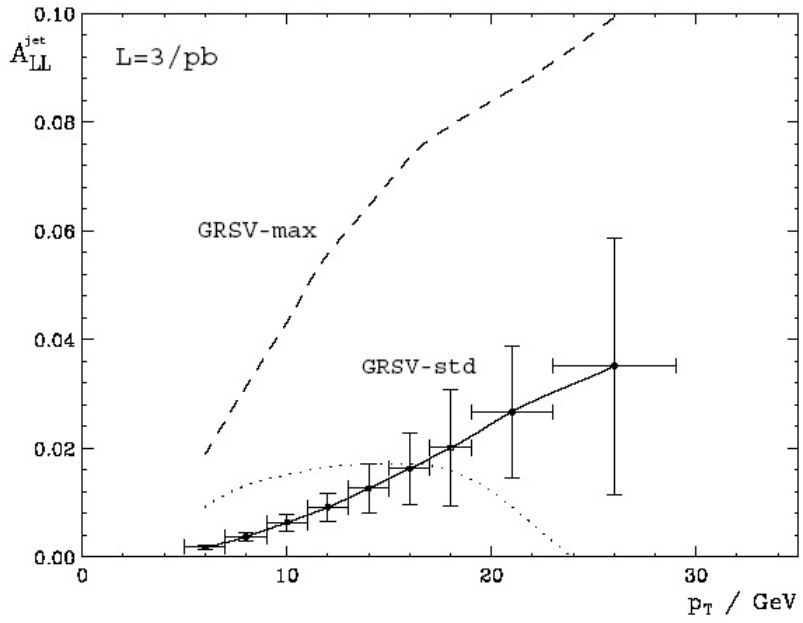

Figure 1.8: Predicted inclusive jet production asymmetries, A_{LL}, are shown above using the inputs of three gluon polarizations. The example gluon polarizations are taken from GRSV's global analysis of pDIS giving a representative range of measureable asymmetries. Both the size and shape of A_{LL} is expected to depend on jet $p_\perp$, and distinguishing between possible input polarizations will require an experimental precision near 1% for many of the bins. The example error bars shown are for a 3 inverse pbarn measurement with 50% polarization. In 2003 STAR sampled 180 inverse nbarns with 30% to 35% polarization, so this analysis's errors will be larger than those shown in picture.

1.8 Summary

This thesis will focus on jet production observed by STAR detector from data taken in 2003. 2003 is the first year RHIC implemented longitudinal proton collisions as well as the first year STAR's Barrel Electromagnetic Calorimeter was available, allowing complete jet reconstruction. These results shown are the first of what will become a comprehensive and multi-year measurement of ΔG.

CHAPTER 2

Experimental Setup

2.1 The Relativistic Heavy Ion Collider

The Relativistic Heavy Ion Collider (RHIC) is located at Brookhaven National Lab (BNL). By connecting a series of accelerators, RHIC is capable of colliding ions as light as protons and as heavy as gold nuclei with one another in its two counter-rotating beam lines. RHIC is particularly impressive due to the broad range of particles it is capable of colliding. Primarily built to provide gold-on-gold (AuAu) collisions with energies up to 100 GeV/nucleon (GeV/u), RHIC successfully achieved this milestone in June 2000. More relevant to this research, RHIC is credited with providing the first ever polarized proton-proton (pp) collisions in a two beam collider, including transversely aligned collisions in 2002, and longitudinally aligned collisions in 2003. To date, the proton collider beams are accelerated up to $\sqrt(s) = 406$ GeV, and in the future the energy will be increased to $\sqrt(s) = 500$ GeV, the design limit of RHIC.

The most notable advantage provided by a two-beam collider over a fixed target experiment derives from kinematics. When fixed target experiments propel protons against a stationary target, much of the usable energy in the reaction is lost, carried away in the forward motion of the incident proton. In an equal-energy two-beam collider, the laboratory frame is the rest frame of the particles' center of mass. The result is that a collision resulting from two head-on 100

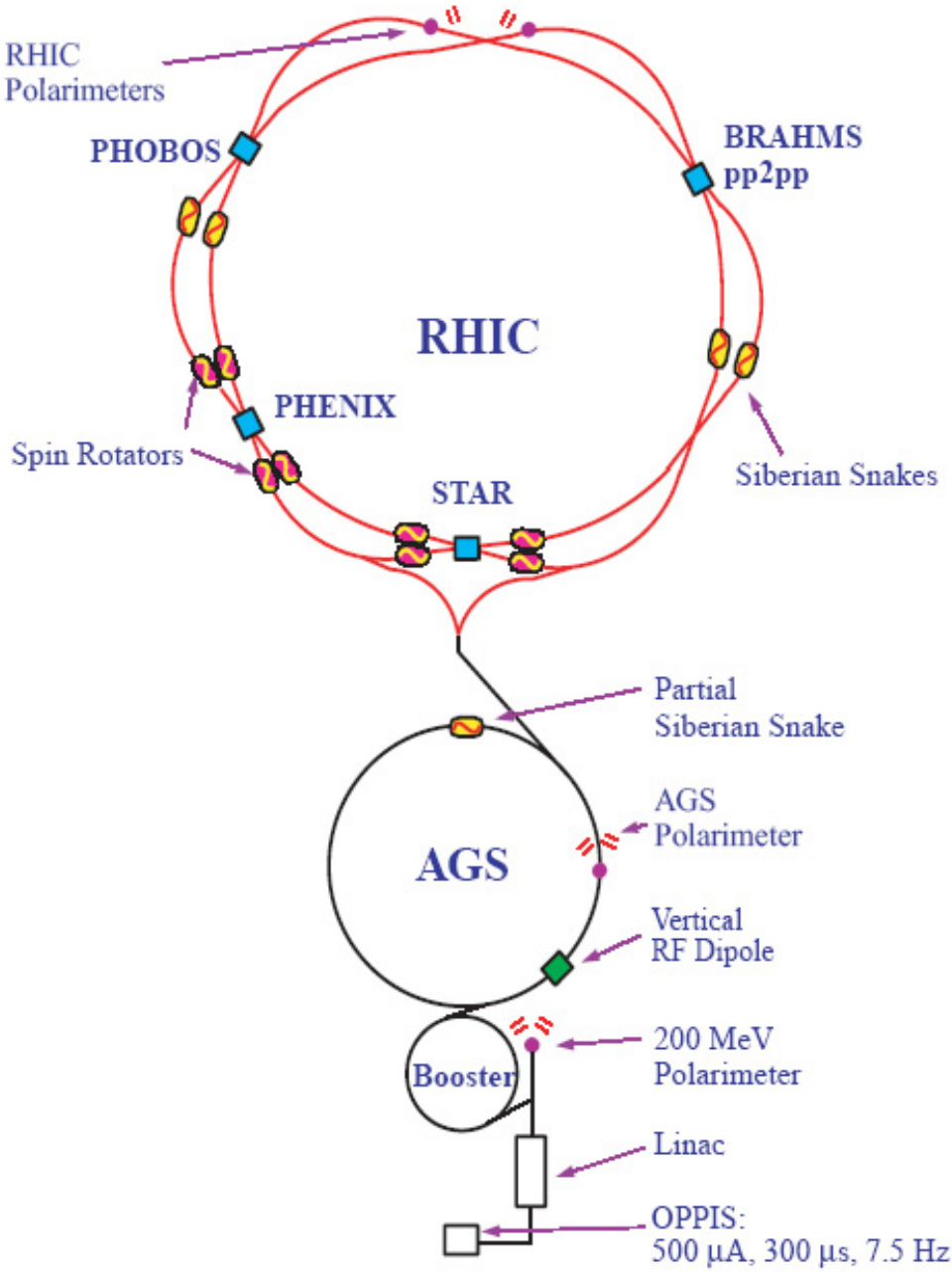

Figure 2.1: A diagram of the Brookhaven National Laboratory collider complex including the accelerators that bring the nuclear ions to RHIC

GeV particles is equivalent to that of a stationary particles being struck by an incident particle with 21,469 GeV of energy. Currently cosmic rays are the only sub-atomic particles observed at such energies.

2.2 RHIC COMPLEX

The RHIC collider is the newest addition to an already well established accelerator complex. Several preliminary stages are necessary to bring stores of particles up to RHIC injection energy, 24GeV. These steps are handled by a series of accelerators.

Acceleration begins at the Optically Pumped Polarized Ion Source (OPPIS). Electrons, polarized by cyclotron resonance, are fed into a rubidium (Rb) cell where they are captured by protons. The Rb cell sits in a 2.5 T magnetic field and is optically pumped by a continuous wave laser. The newly formed hydrogen atoms then pass through the cell into a changing magnetic field called the Sona transition region. Here the electron's polarization is transfered to the proton. While traversing a sodium vapor cell, electrons are then added to the protons creating an ionized Hydrogen beam. The polarization of H- beam is typically near 80%.

Once polarized, the beam is passed into a radio frequency quadrupole preinjector before passing into a series of nine radio frequency cavities. The cavities raise the beam's energy to 760 keV before feeding the ions into the LINAC, a linear accelerator spanning the length of a 459-foot tunnel.

LINAC-produced 200 MeV protons are now led into the Booster synchrotron where they are accelerated to a total energy of 2.4 GeV, and passed into the Alternating Gradient Synchrotron (AGS).

Figure 2.2: The linac

The AGS, built in 1960, once served as Brookhaven Lab's premier accelerator, and became well known for the three Nobel Prizes won as a result of the research performed there. These includes the co-discovery of the J/ψ in 1976 by Samuel Ting, the first observation of CP violation in 1989 by Cronin and Fitch, and lastly the discovery of the muon-neutrino in 1988 by Lederman, Schwartz and Steinberger. The AGS implemented an at the time new technology dubbed alternating gradient focusing, in which field gradients of the accelerator's 240 magnets are successively alternated inward and outward. These field alterations cause particles to be focused in both the horizontal and vertical plane at the same time. The AGS is capable of accelerating 25 trillion protons with every pulse. Protons accepted from the Booster Ring into the AGS are accelerated to 24 GeV before injection into the RHIC collider.

In the existing setup, the AGS and RHIC are decoupled. One benefit of this decoupling is that beams can be prepared for RHIC injection while RHIC is

still conducting collisions. The direct implication is a reduction in the downtime separating a RHIC beam dump from a re-injection by the AGS.

2.3 RHIC

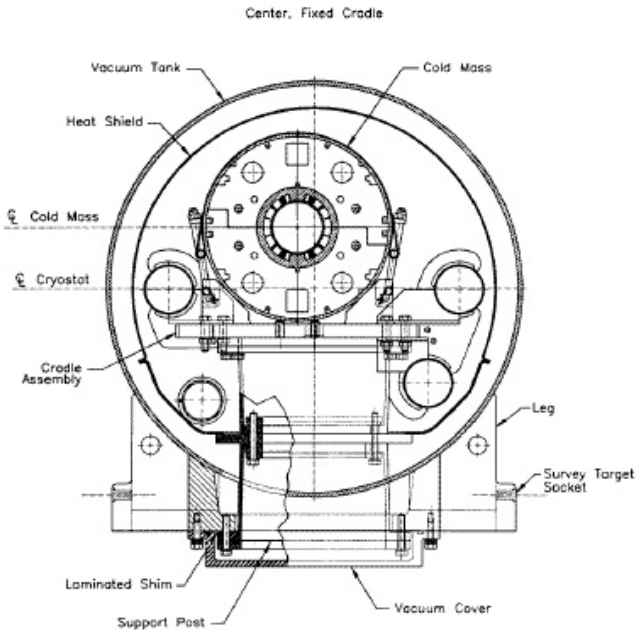

Figure 2.3: An arc dipole magnet from the RHIC beam line. Cryostats enclosements are necessary for the superconducting magnets.

The RHIC facility consists of two rings of superconducting magnets, each measuring 2.4 miles in circumference. The main components of the magnet system are 288 arc dipoles, 108 insertion dipoles, and 276 arc and 216 insertion quadrupoles. In addition to the dipoles and quadruples, an inventory of 72 trim quadrupoles, 288 sextapoles, and 492 corrector magnets exist.

An arc dipole magnet is shown in Figure 2.3. Each dipole structure has a physical length of 9.782 meters, bends with a 4.85 cm sagitta and has a coil aperture of 8 cm in order to accommodate intra-beam scattering. The beam

tubes in the magnets are at liquid helium temperatures, with the beams in the arcs separated by 90 cm. The magnets are cooled to a temperature of < 4.6 K by circulating super-critical helium supplied by 24.8 kW refrigerators. Extremely good vacuums of $< 10^{-11}$ mbar in the cold bore and 7×10^{-10} mbar in the warm beam tube sections are achieved at RHIC to minimize beam losses and radiation background.

When beam is received from the AGS, it arrives in bunch form. RHIC is capable of storing up to 112 bunches in each ring, however in 2003 only 56 bunches were filled. To accelerate, capture and store the beam bunches, RHIC employs a radio frequency (rf) system [Pro94]. From beam injection, an acceleration system (26 MHz) captures the beam, brings it to full energy (100GeV/u) and performs bunch shortening. A separate storage system operating at 196 MHz is then employed to maintain the beam's integrity. Lastly a longitudinal kicker system is required to act as a dampener when longitudinal injection errors occur, and when neighboring bunches couple.

Of the six interaction points present at RHIC, four are used by experimental collaborations. BRAHMS, PHOBOS, PHENIX and STAR are all independent experiments with differing observation ranges and equipment. A large overlap exists between the experiments measuring capacities allowing for cross checks and references.

2.4 Beam Polarization and Spin Dynamics

While the protons are accelerated and stored in the AGS and at RHIC, their spins are aligned transversely to the beam's direction. *Spin rotators* located just before and after the STAR interaction region rotate the beam's spin axis from

the transverse into the longitudinal direction. The beams remain in longitudinal polarization only in the collision region and are then rotated back into their transverse orientations. When the spin is transversely oriented, and thus aligned or anti-aligned with the magnetic field, beam polarization is stable while standard spin precession occurs. When circulating around the accelerator, if the spin's axis wanders into the longitudinal and normal directions depolarization occurs. Assuming that the accelerators have no electric field and that their magnetic field, B, points only in the transverse direction, the equation of motion for the circling proton are

$$\begin{aligned} \frac{d(\vec{v})}{dt} &= -\frac{e}{m\gamma}\vec{B_{\perp}} \times \vec{v} \\ \frac{d(\vec{S})}{dt} &= -G\gamma\frac{e}{m\gamma}\vec{B_{\perp}} \times \vec{v} \end{aligned} \tag{2.1}$$

The term $G\gamma$, often written as ν is the called the spin tune, and describes how much faster the proton's spin precesses in comparison to its orbital motion. For example, if the spin tune is 2 then the spin precesses twice with every revolution around the accelerator.

When the spin tune is in phase with a perturbing effect, the perturbation will rotate the spin into a normal or longitudinal direction causing depolarization to occur. One type of perturbing effect is an imperfection resonance. Imperfection resonances often occur from magnet misalignments or closed orbit errors; problems occurring from the imperfections may be minimized but are nevertheless unavoidable. These resonances occur when spin tune is equal to an integer, n.

$$\nu = G\gamma = n \tag{2.2}$$

To guard against these conditions Siberian snakes and quadrupole magnets are employed. These devices generate a strong perturbing magnetic field in a single region. This field causes a moderate spin rotation, not large enough to affect the spin's stability under normal conditions. However when the spin tune equals an integer, the induced perturbation causes a complete spin flip. By flipping the polarization 180°, a spin previously aligned with the accelerator's magnetic field becomes anti-aligned and vice versa. Since the spin axis only points in unstable orientations for only a short while, polarization loss is minimal.

Several other types of depolarizing resonances occur throughout the protons ramp, all of which are handled in a manner similar to the one outlined above. In total polarization degrades from $\sim 80\%$ at OPPIS, to $\sim 30\%$ in the RHIC ring at time of collisions and data taking. These losses are being studied with hopes of eventually achieving $\sim 70\%$ polarization by the program's maturity. Most of these gains will be realized through stronger Siberian snakes placed in both the AGS and RHIC facilities.

2.5 Polarimetry

A polarimeter is a device capable of measuring a specific asymmetry, this measured asymmetry is then used to describe the polarization of the tested beam. The RHIC facility hosts several polarimeters, and each polarimeter preforms a specific task. The tasks may be grouped into three categories. The first is making a relative measurement of the beam's transverse polarization. Longer term polarimetry experiments provide the information needed to normalize/map the relative polarization into an absolute polarization. Thirdly, a local polarimeter at the collision region is necessary to ensure that the polarization's axis is completely rotated from the transverse to the longitudinal direction.

Two fast polarimeters are used to make the relative polarization measurements, these measurements are used to determine the beam's instantaneous polarization. One polarimeter is located in the AGS, and the second is located in the RHIC facility. By observing proton-carbon elastic scattering in the so called Coulomb Nuclear Interference (CNI) region, these CNI polarimeters measure the beam's relative polarization to within a statistical accuracy of $\pm 5\%$ in a only a few minutes. Day to day run operations also rely heavily on the CNI polarimeters to observe sudden drops in beam polarization and to perform systematic studies of beam loss occuring during the ramping process.

The results of two experiments are used to map the measured relative polarization into an absolute polarization. Results from the E880 polarimeter, located in the AGS, are used to determine AGS beam polarizations and are used to estimate RHIC polarizations to within $\pm 30\%$. This error is primary due to extrapolating the E880 results using 24 GeV protons to RHIC's CNI polarimeters results using 100 GeV protons. More recently a hydrogen gas target with polarized protons was placed in the RHIC ring. In 2004, results from this hydrogen target reduced the error on the absolute polarization to from $\pm 30\%$ to $\pm 10\%$. Our results use the final values as determined by the gas jet polarimeter.

Finally the Beam Beam Counters (BBC), which will be described in Chapter 3, are STAR's local polarimeters. The BBC may be used as a local polarimeter during transverse running and as a local null-polarimeter during longitudinal running. When the spin rotators are not active (thus the beam is transversely polarized), the BBC can quickly measure a non-zero asymmetry occurring from forward charged particles production in proton collisions. When the spin rotators are engaged, if both the transverse and normal (left-right or top-bottom) asymmetries are measured to be zero, then any existing beam polarization may

only be directed into the longitudinal direction. Alone this information does not guarantee longitudinal polarization. However when coupled with a positive polarization measurement from the CNI, the tipping angle away from the longitudinal direction at the collision region can be determined to within the errors of the combined measurement.

CHAPTER 3

The STAR Detector

This experiment was performed at the Solenoidal Tracker at RHIC (STAR). STAR is a large-acceptance set of detectors designed to study a broad range of physical observables. The cylindrical STAR structure hosts several sub-systems, nearly all of which cover the complete 2π in azimuth, and is housed within a 0.5 Tesla magnet. By design, an emphasis was placed on mid-rapidity physics, a region which encompassing numerous topics of great interest to both the spin and heavy ion physics communities. The primary sub-systems of STAR are shown in figure 3.1.

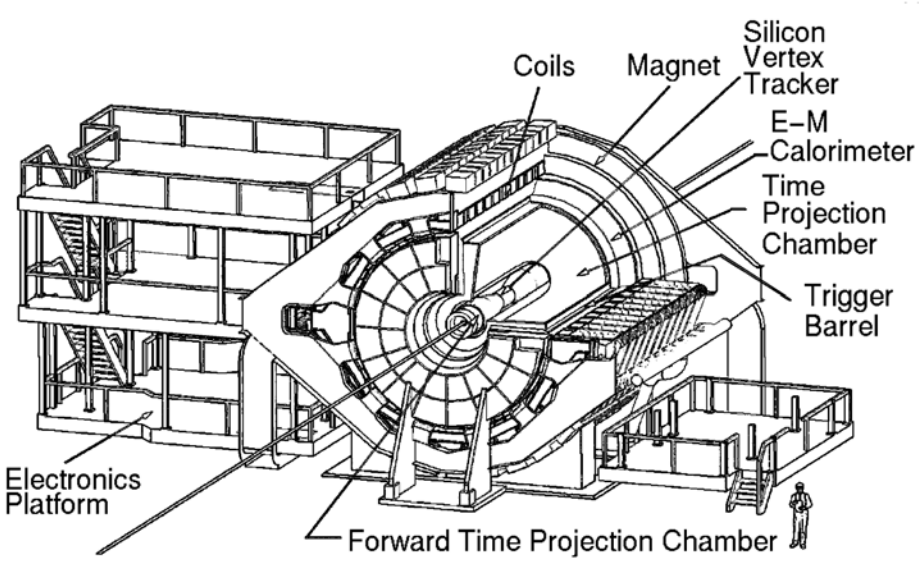

Figure 3.1: View of the STAR detector system. The line protruding outward depicts the beams' path.

The first and arguably most important step in data acquisition is to determine when the detectors should be actively recording data. Depending on one's physics objective, different classes of collisions may be of interest. In principle this can be achieved by linking any sub-system to the triggering system, and in practice nearly every sub-system does at some point take part in this process. Here, preferential treatment is given to detectors used in this analysis.

At the minimum, one would like know if a collision did occur and if so, will its remnants be observable by the main detectors. For a proton-proton collision two detector sub-systems are used to select these *minimum bias* events, the Beam-Beam Counters (BBC) and the Central Trigger Barrel (CTB). The Barrel Electromagnetic Calorimeter (BEMC) provides a more selective trigger useful for high $p_\perp$ physics, such as jet finding.

3.1 Beam Beam Counters

The Beam Beam Counter (BBC) is serves many purposes at STAR. First, it measures the absolute luminosity of the incoming protons by counting the number of collisions occurring throughout the entire running period. Second, it monitors the relative beam luminosity, this is the ratio of collisions found between the different spin orientations. Both quantities are essential to the analysis. Finally, during transversely polarized proton running the BBC acts as a local polarimeter. The polarimeter aspect of the BBC cannot be under emphasized. Without being positive that polarization is strictly in the longitudinal beam direction, the value of measurement toward understanding the gluon's polarization is lost.

The Beam Beam Counters are a pair of highly segmented annuli consisting of small and large hexagonal tiles of scintillator. The counters are mounted around

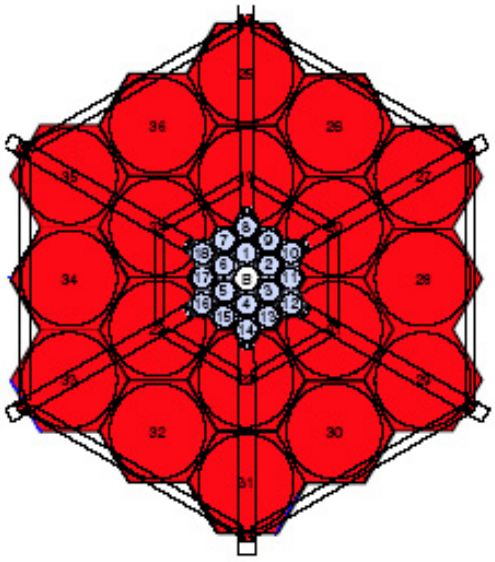

Figure 3.2: Two BBC units are installed at STAR, each is centered along the beam line 3.7 meters from STAR's center. The small hexagonal scintillators found in the center of the BBC, when fired in coincidence, observe 26.1 $mbarns^{-1}$ of the proton cross section. The BBC's are used to normalize the unpolarized jet cross section and determine the relative luminosities of the spin-sorted beam.

the beam pipe beyond the east and west pole-tips of the STAR magnet, 3.7 meters from STAR's center. The 2x18 arrays of small hexagonal tiles have an inner radius of 9.6 cm and an outer radius of 48 cm, corresponding to a psuedorapidity range of $3.4 < |\eta| < 5.0$. The 2x18 arrays of large hexagonal tiles span 38 cm to 193 cm in diameter, corresponding to a psuedorapidity range of $2.1 < |\eta| < 3.6$. The small hexagonal times were read out with 2x16 and the large with 2x8 photo multiplier tubes.

The scintillators of the BBC are mainly sensitive to charged particles. For every bunch crossing the BBC sums the signals from its small scintillators; one sum for from the East and one from the West detector. If both signals exceed a given threshold and fall within a 17 ns time coincidence window, the event is accepted for further consideration. Another condition must be satisfied by the Central Trigger Barrel (CTB) for the event to be considered a minimum bias event. The 1 ns timing resolution of the BBC can be used to preferentially select events within a 60-cm region in z. However this feature was not implemented during the 2003 proton proton run.

3.2 Scalar Boards

The scalar boards are a fast readout system (9.37 MHz) used in conjunction with the BBC. The STAR system has six scalar boards, each with 24 input bits: 7 to store the bunch crossing number and 17 for detector information. An important example of a bit used to store detector information is the bit used to store the BBC coincidence condition described above. At RHIC the beam is typically separated into 56 (or 112) bunches in each ring for a total of 56 (or 112) bunches crossings. Since the number of protons, and spatial arrangement of protons is not uniform from bunch to bunch, some bunch crossings are more likely to produce collisions

than others, ei., have larger luminosities. When performing spin asymmetry measurements, properly accounting for these luminosity differences is imperative to insure that false asymmetries are not observed. The relative luminosities of the bunch crossings are recorded every few minutes throughout the data taking, and used in the analysis to remove false asymmetries.

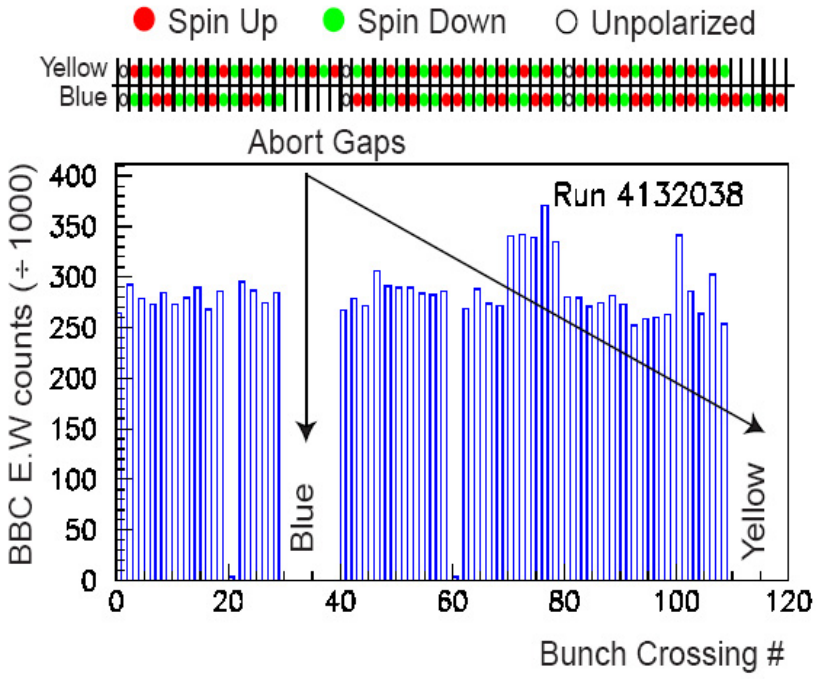

Figure 3.3: Above is a RHIC fill spin pattern. Below, the BBC coincidences are plotted for each proton bunch.

3.3 Time Projection Chamber

The Time Projection Chamber (TPC) is the paramount detector at STAR. Currently the largest such device built, the STAR TPC's detection chamber is 4.2 m long, 2 m in inner diameter, and 4 m in outer diameter. This drift volume provides for a large particle acceptance, such that the TPC can efficiently reconstruct charged particles in the range of $|\eta| < 1.6$ and the full 2π in azimuth.

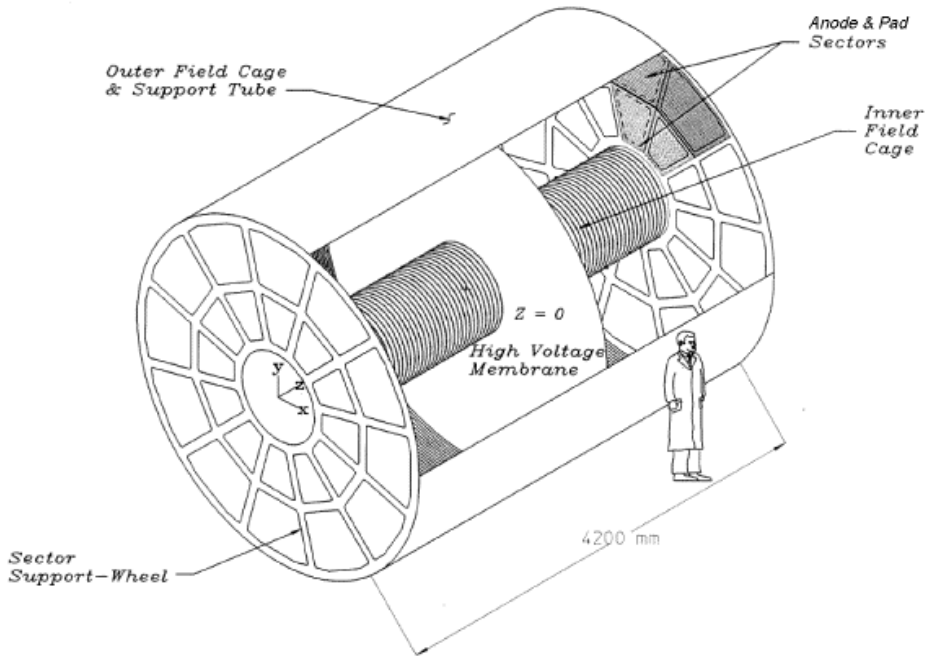

Figure 3.4: Sectioned view of the STAR TPC showing the inner/outer electric field cage, the central membrane, and the inner and outer sectors.

The chamber is filled with P10 gas (a 10% Methane and 90% Argon mixture), as well as longitudinal electric and magnetic fields. The strong magnetic field bends the paths of charged particles as it traverses the chamber, creating a helixical curve. As the particles proceed through the TPC, they ionize the P10 gas, leaving a trail of electrons. These electrons then drift toward a detector pad on the outer walls of the cylinder where their signal is recorded. The signal is later reconstructed giving the original particle's position and momentum vectors. The curvature path resulting from the magnetic fields interaction with the particle is then used to determine the particle's momentum. To first order, the motion of a particle passing through a uniform magnetic field adheres to the straightforward relation

$$p = qRB \tag{3.1}$$

where p is the particle's momentum perpendicular to the field's direction, q is the particles electric charge, R is the radius of the resulting circle and B is the field's magnitude. Several corrections must also be applied. Most notably an $\vec{E} \times \vec{B}$ correction is necessary because the electric and magnetic fields are not precisely perpendicular throughout the entire TPC. Secondly, a *space charge* correction is applied to compensate for the pile-up of positive charge from slow-moving ions that remain near the collision region. As these gas ions diffuse toward the central membrane new ions take their place, the resultant effect is a $q(r,z) \sim \frac{1}{r_{cylindrical}}$ charge density that alters the path of other charged particles from a perfect helix.

A central membrane cathode constructed from kapton is held at 28 kV and the shield grids at the end-caps are held at ground. A chain of 183 resistors and equipotential rings are placed along the inner and outer radii to maintain the

uniformity of the electric field. The resultant field guides the trail of electrons to the end-plates at a drift velocity of 5.45 $\frac{cm}{\mu s}$. Upon reaching the end-plates 136,608 pads are available to record the position and arrival time of the drift electrons.

3.4 Central Trigger Barrel

The Central Trigger Barrel is a fast detector used for event triggering and TPC track selection. Much like the BBC, the CTB is a scintillator based detector used to count charged particles and covers the complete 2π in ϕ. The CTB covers a psuedorapidity range of $|\eta| < 1$ with 240 scintillating slats arranged in 4 cylindrical bands. Although the 4x60 slats give poor position resolution and no momentum resolution, the fast timing resolution can be used in conjunction with the TPC's accurate position and momentum to better understand an event.

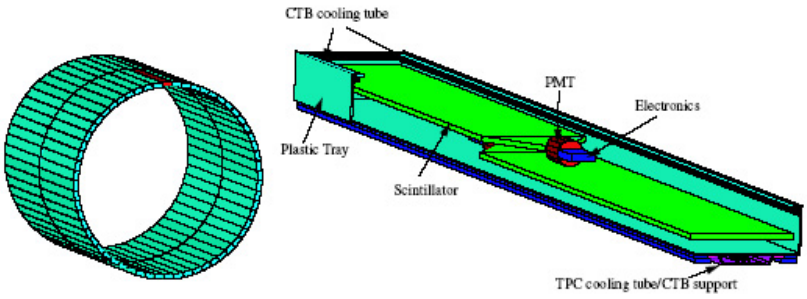

Figure 3.5: The right hand schematic depicts a scintillator slat of the CTB. The plastic slats have low granularity, but fast timing resolution, and are often used in conjunction with the Time Projection Chamber. On the right the ensemble of slats is presented as used at STAR.

As previously mentioned, the TPC needs 40μs to read out an event due to the finite drift time of the track's electrons. During this time other charged particles may pass through the TPC volume. When these additional tracks are read by

the TPC, they are included with the original event's track, corrupting the event's purity. There are three primary sources of contamination: beam-gas interactions, cosmic rays, and other real collisions occurring at a nearby time and position to the triggered collision. Fortunately the CTB provides a reliable method to filter these tracks from the tracks of the triggering collision. By matching TPC tracks to CTB slats, the CTB's timing resolution can be used to augment the TPC's information. When determining the vertex position only tracks in time with the collision, as determined by the CTB's timing, are considered.

3.5 Barrel Electromagnetic Calorimeter

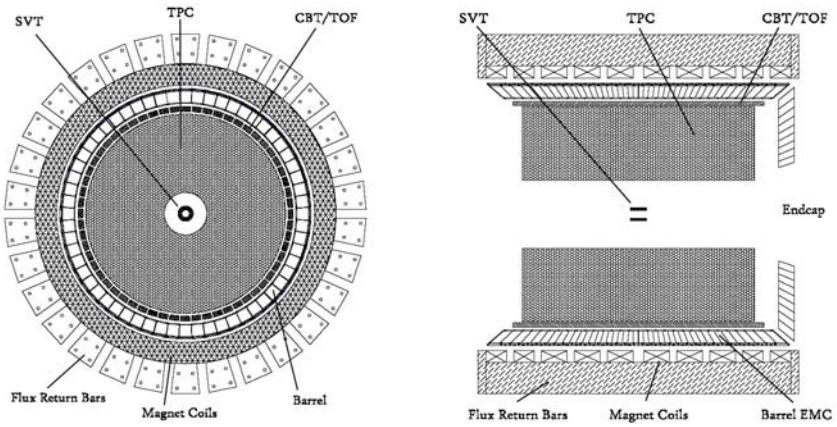

Figure 3.6: Cross sectional views of the STAR detector. The Barrel Electromagnetic Calorimeter is located between the TPC's gas chamber and the 0.5 Tesla magnet used to bend charged particles as they traverse the TPC's gas chamber.

In 2003 the West half of the Barrel Electromagnetic Calorimeter (BEMC) was installed and instrumented, providing coverage from 0 to 1 in η, and the full 2π in ϕ. The BEMC is a sampling calorimeter consisting of alternating layers of lead and plastic scintillator. The half calorimeter is divided into 60 modules, each sub-tending 6° in ϕ and spanning the full unit in η. Each module is ~ 26

cm long and $\sim$ 293 cm long with an active depth of 21 radiation lengths ($X_\circ$).

Each module is further divided into 40 towers, 2 in ϕ and 20 in η, with each tower being 0.05 in $\Delta\phi$ and 0.05 in $\Delta\eta$. The half calorimeter is thus 2400 towers, and when fully installed the whole calorimeter will contain 4800 towers. Each tower is projective in that it points toward the interaction region as shown in figure 1.7. This projection allows the cylindrical build of the BEMC to mimic the spherical geometry natural to a collision.

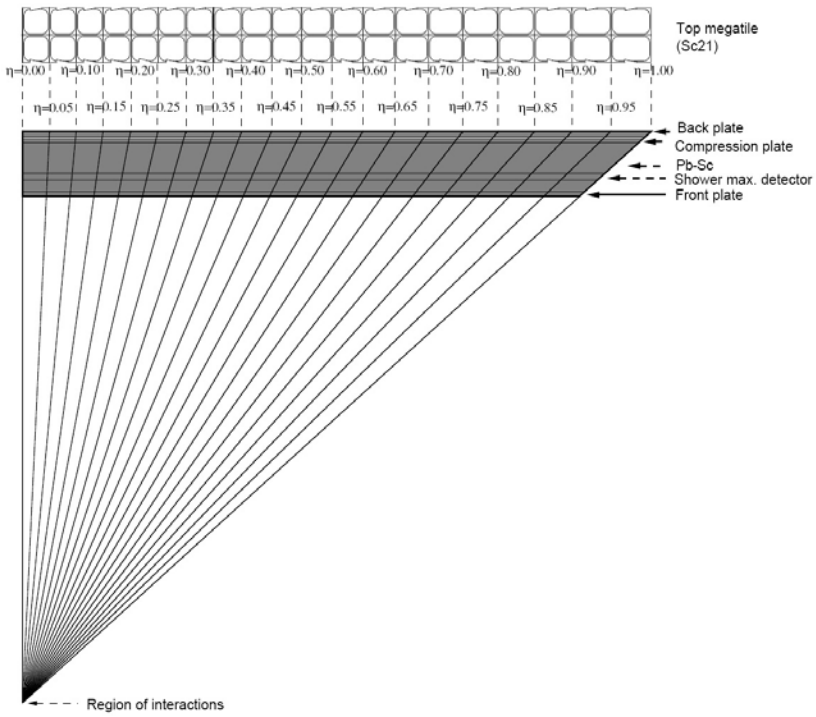

Figure 3.7: Side view of a calorimeter module showing the projective nature of the towers. Because only half of the calorimeter was installed, the left hand side, $\eta = 0$, corresponds to the center of the STAR detector.

The towers consist of 20 layers of lead and 21 layers of scintillator. The lead layers are each 5 mm, and the 19 layers of active scintillator strips used in 2003 are also 5 mm. Two 6 mm layers of scintillator located in the front of the stack are

used as a preshower detector, however they were not instrumented until 2004. The BEMC also contains a Shower Max Detector (SMD). The SMD is highly segmented and located $\sim 5X_\circ$ inside the BEMC. The SMD strips, each $\sim$ 2 cm wide, provide refined position resolution and are also capable of determining the shower width of incoming particles. This shower width becomes particularly important when trying to differentiate high energy neutral pions from high energy direct photons.

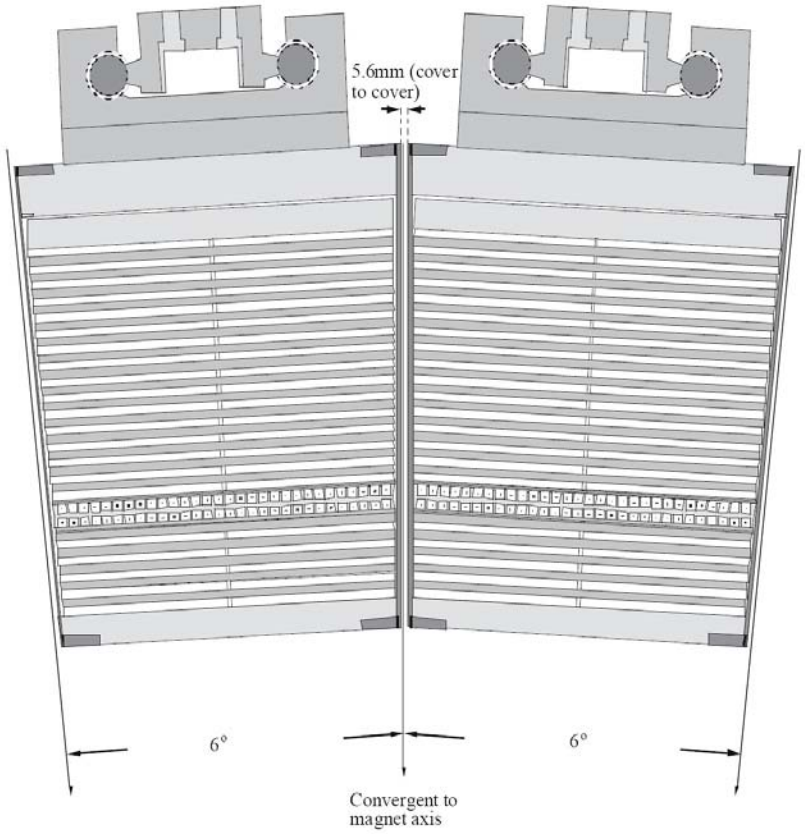

Figure 3.8: The end view of two calorimeter towers. The alternating layers of lead and scintillator make up the bulk of the detector. The SMD provides higher position resolution and is located at a depth corresponding to the expected peak in the electromagnetic shower.

The BEMC's response is highly dependent on the type of particle which passes

through it. Its greatest sensitivity is to photons and electrons, as they interact with the lead layers almost immediately upon entering the detector. The two most common neutral mesons, $\pi 0$'s and η's, both have primarily decay channels into photon pairs. Since the BEMC is sensitive to the photons, the neutral mesons can be identified by reconstructing their Lorentz-invariant masses from photon pairs, making the BEMC sensitive to these neutral mesons as well.

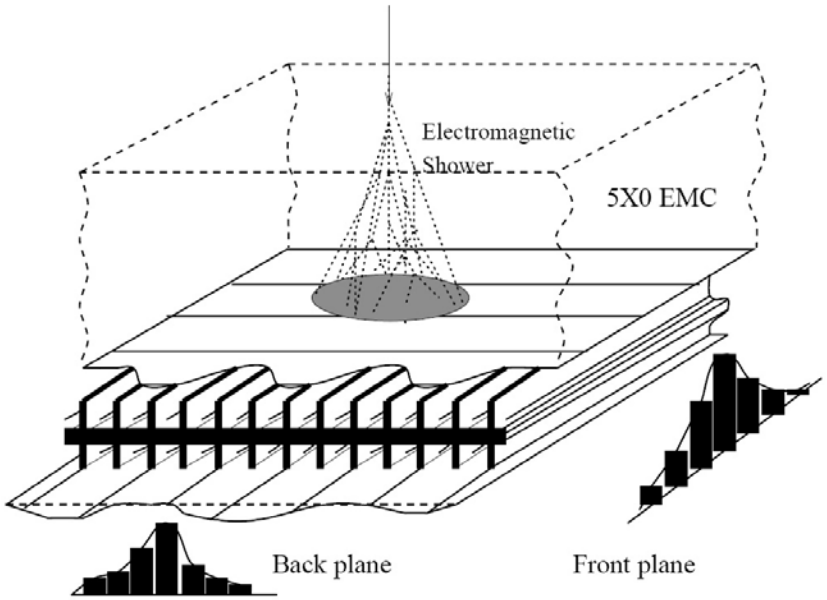

Figure 3.9: Pair production occurring from high energy photons and electrons striking the lead layers create electromagnetic showers within the detector. An idealized response from the SMD strips is projected from the shower.

Charged mesons (π^+ and π^-), protons and neutrons are less affected by the electromagnetic interaction with the lead atoms because their mass is considerable larger than that of an electron. Often these particles will pass through the entire detector and only deposit a small and relatively constant amount of energy, typically 300 to 350 MeV, depending on the incident angle of the particle on the calorimeter. Particles depositing only this minimum energy are collectively called MIPS (Minimum Ionizing Particles). Alternatively, these particles

may interaction with the lead nuclei, creating a hadronic shower, and depositing some fraction of the particles energy into the calorimeter. Anti-protons and anti-neutrons may also interact with lead nuclei. In these cases the antimatter and matter annihilate depositing an additional energy equal to twice their rest mass of the nucleon, ~ 2 GeV.

A photon's initial electromagnetic interaction with the calorimeter's lead layercreates an electron-positron pair through pair production. The electron-positron pairs quickly interacts with the high Z lead radiating Bremsstrahlung photons. The photons, electrons, and posititrons continue to populate the calorimeter, growing in number through pair production and Bremsstrahlung radiation, creating an electromagnetic shower. For energetic particles, the resulting shower of charged electrons and positrons peaks near $5X_\circ$ into the detector (where the SMD is positioned) and dies out before exiting the detector. The BEMC is designed to record particle energies as great as 60 GeV in a single tower. Although physically possible, essentially no photons or electrons with this amount of transverse energy are produced in $\sqrt{s} = 200$ GeV proton collisions.

As the electron and positiron shower passes through the scintillator layers, it interacts with the scintillator, emitting low energy, 5 eV, photons. The photon signal from each scintillator tile is readout through a wavelength shifting (WLS) fiber embedded into a $'\sigma - groove'$ that is machined into the tile. Finally all 21 WLS fibers from a tower are fed into a single Photo Multiplier Tube (PMT).

The magnitude of the PMT's response is linearly related to the energy of the incident photon/electron striking the tower, and the coefficient relating the two quantities is called the gain. The gain is determined through a combination of measurements. MIPs are used to establish a relative gain between the 2400 towers and to set a nominal absolute gain. Once all towers are calibrated to be internally

consistently, an absolute calibration is performed using identified electrons. The electrons momenta are well determined from the TPC and matched to the towers' energy response.

CHAPTER 4

Data used in Analysis

4.1 Data

In 2003 RHIC collided longitudinally polarized protons over the course of two weeks. During this time STAR implemented two primary triggers while sampling approximately 300 inverse nanobarns (nb^{-1}) of delivered collisions. The first trigger recorded generic events and the second observed a more exotic subset of the generic events.

As a quick review of the naming conventions used, proton collisions are typically called *events*. Events that satisfy triggering conditions are recorded in blocks called *runs*, and a typical run contains 100-200k events. Finally, every time fresh beams are put into the collider, a new *fill* or *store* begins. So, over the course of a fill STAR takes several runs and records many thousands of events.

The generic trigger implemented is the minimum-bias trigger. The minimum-bias trigger attempts to observe all types of collisions in proportion to the likeliness they occur. Few of these collisions will produce jets in the energy and spacial region of interest to this analysis. Nonetheless this data provides a base useful for performing systematic studies and is also be used as a reference to normalize the exotic trigger to the absolute cross-section.

Ideally every minimum-bias trigger issued would be recorded for analysis. Un-

fortunately the data acquisition (DAQ) system is limited to a maximum recording speed of approximately 100Hz and the rate of incoming minimum-bias triggers ($\sim$ 30 kHz) far exceeds the DAQ's and the detectors capabilities. A more selective trigger is set to fire at a rate comparable to that of the DAQ rate. The second trigger selects only those minimum-bias events also containing at least one tower from the BEMC exceeding an ADC threshold equivalent to 3.5 GeV in transverse energy. This trigger is characteristically named the "high tower trigger", and events of this trigger are far more likely to contain jets useful for analysis.

When reading out data the trigger pauses, and does not look for further events until the the data is finished reading out. In STAR's case, if the trigger records data at a rate of 1 Hz from it's 100 Hz capability, the detector is *dead* for 1% of the time, and *live* for 99% of the time. This complicates the goal of recording as much interesting data as possible. A very selective trigger records fewer events, but is live for a substantial amount of the time, seeing nearly all of the most interesting (higher energy threshold) data. Alternatively a less selective trigger might record data at 90 Hz and would then be blind to 90% of the events occuring. The result would be 90 times as many events recorded as the selective 1 Hz trigger, but also 10 times fewer of the most energetic events. At STAR the decision made was to run the detector half live and half dead, i.e. near 50 Hz. Typically 4000 minimum-bias events occurred for every high tower event selected.

Trigger Type	Number of Events Recorded Prior to Cuts
Min-bias	1.0×10^6
High Tower	1.5×10^6

Table 4.1: The number of proton-proton events used in the analysis.

4.2 The Collision Vertex

The two proton beams are steered with the intention that collisions will occur at the center of STAR detector. In the case of the TPC, this generally increases the length of a charged particle's path within the TPC's volume, giving a better momentum resolution. Likewise, as mentioned in chapter 3, the BEMC is designed to detect particles originating from the center of the STAR, increasing the chance that a particle's energy is deposited into a single tower. For these reasons we prefer to analyze data near the detectors center. Conversely we would like to retain as much data as possible. From these competing factors, this analysis places an ad hoc cut to be applied to the collision interaction point. Events are only selected if a collision vertex is reconstructed between $+75$ and -75 cm from the center of the STAR magnet.

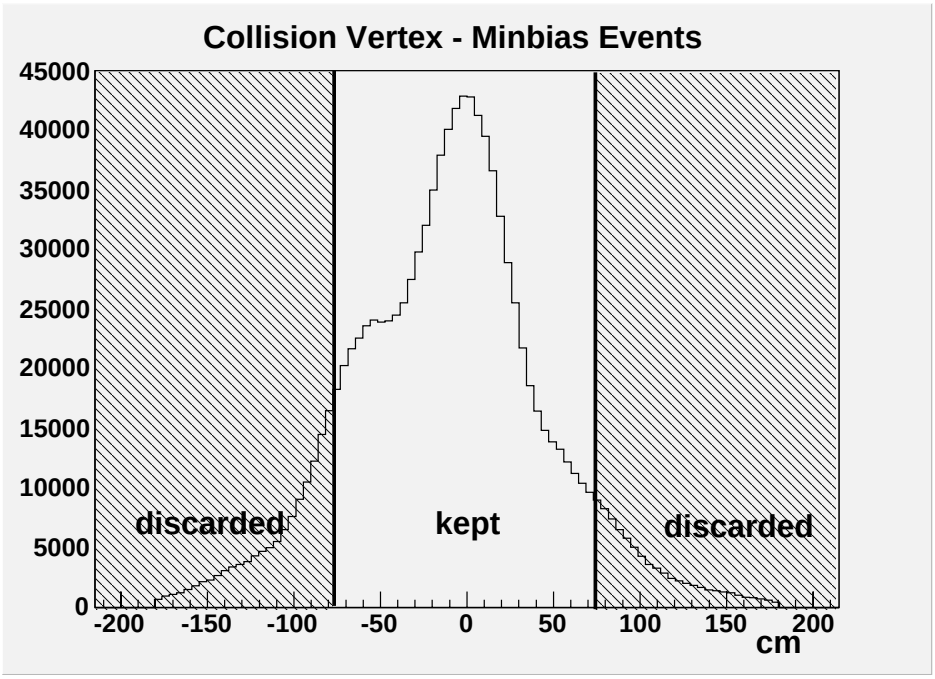

Figure 4.1: The distribution of collision vertexes for minimum bias events.

From figures 4.1 and 4.2 an apparent asymmetry exists in the collision vertex

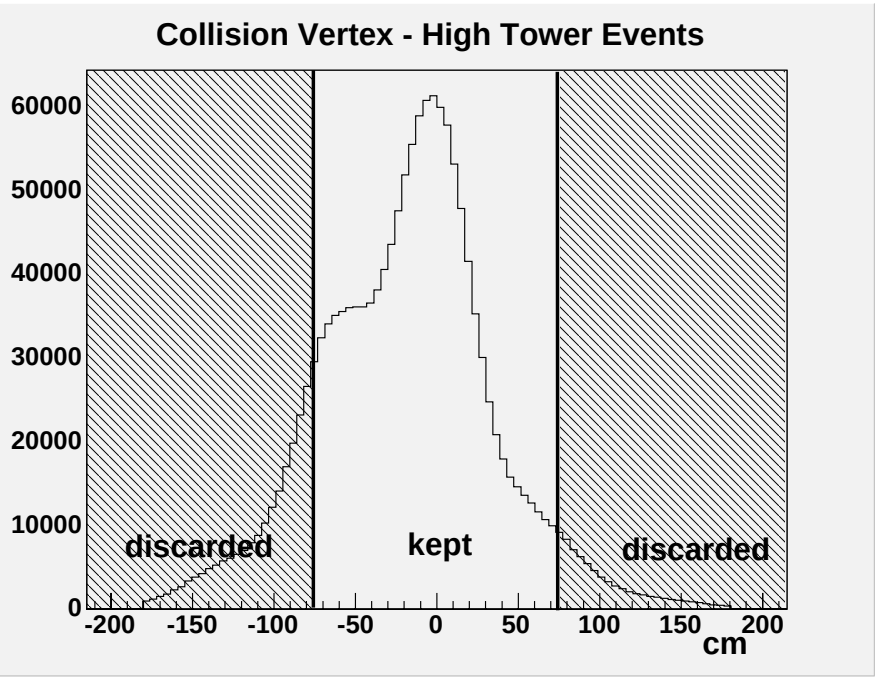

Figure 4.2: The distribution of collision vertexes for BEMC high tower triggered events.

location in the form of a second peak occurring in the negative z region. Examining this on a day-by-day basis for the high tower triggered data, a clear time dependence is observed, as seen in Figure 4.3. On days with an asymmetry, the observed second peak appears Gaussian in shape - a secondary interaction site.

The double structure seen in the vertex distribution could occur for two reasons. Since each beam is composed of 56 bunches, the case could be that some bunches were mis-aligned and collided at a different places than the rest of the bunches. The second possibility is that some beam particles are present around each bunch. These residual particles could form a halo in front of and/or behind the main bunch and interact with the incoming bunch from the oppsoing ring, creating a non-guassian or asymmetric distribution. In Figure 4.4 the collision vertex is presented for each bunch crossing from the data taken on day 137. The common presence of the double peak structure suggests a beam residual.

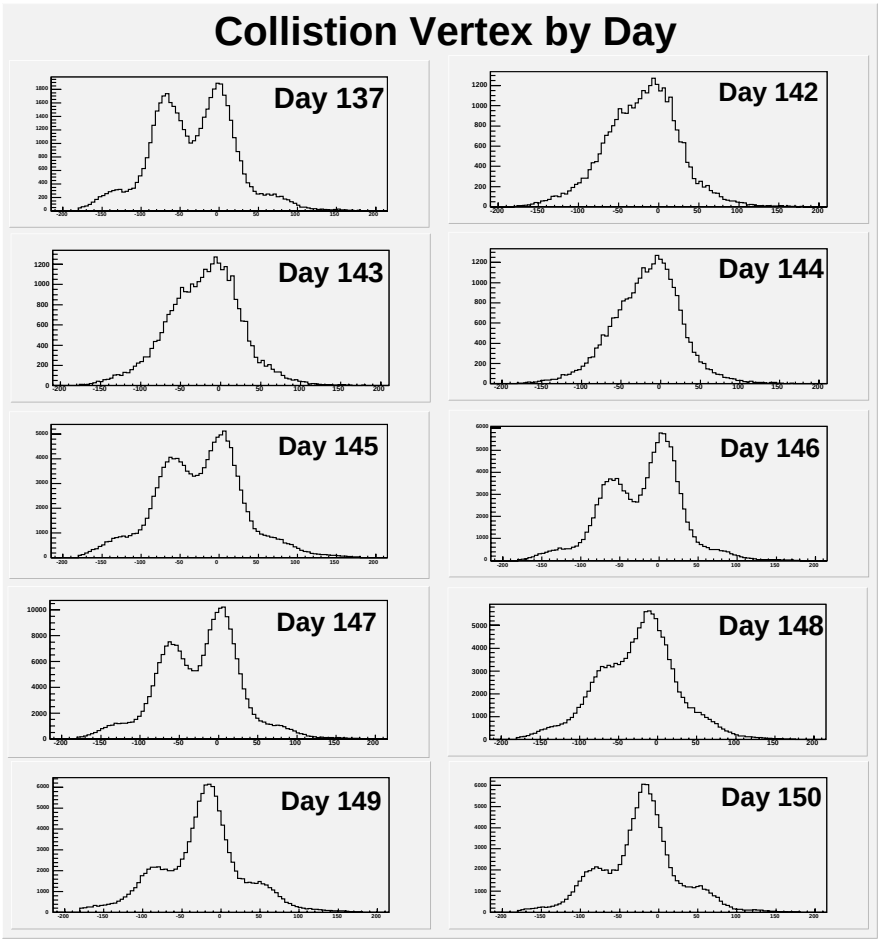

Figure 4.3: The 2003 run lasted for two weeks. By looking at the collision vertex one day at a time we see that the double structure appears in some of the collision bunch crossings, but is absent in others.

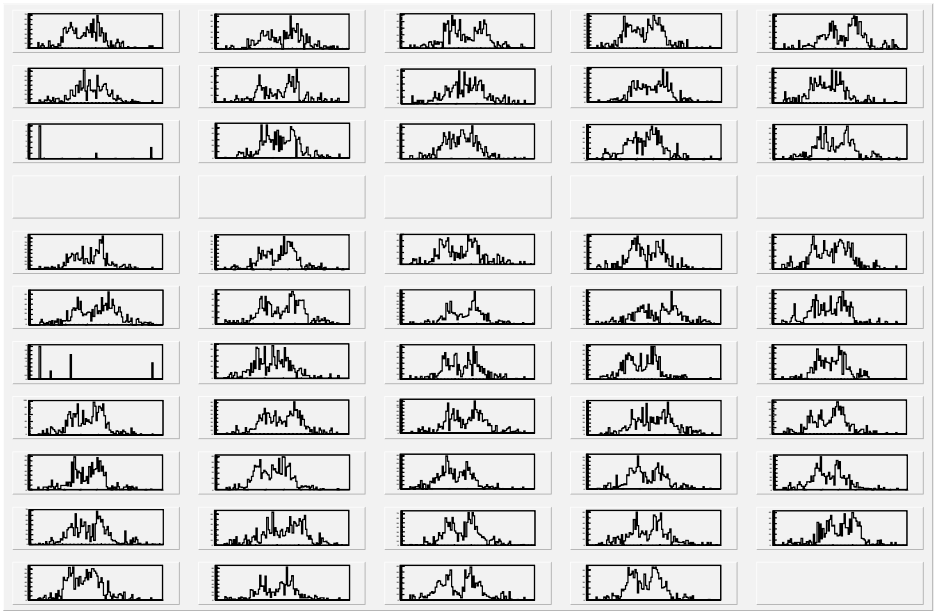

Figure 4.4: The first day of the data recording (day 137) exhibits a double peak in the collision's z vertex. In each beam, 56 (of the possible 112) bunches of protons were filled, stored and collided with an associated bunch from the opposing beam. The collision vertex of the resulting 56 bunch crossings are shown above in order beginning at the top left. The empty plots indicate unfilled bunch crossings that may result from either one or both of the beam's bunches not being filled. The observant reader will notice that only 55 graphs are plotted - bunch crossing 56 is not shown and is also unfilled. The double peaked structure is present throughout the 56 bunch crossings.

4.3 Quality Assurance of Detector's Performance

A preliminary round of quality assurance (QA) checks are done to ensure that the primary detectors (the TPC, BBC, and BEMC) are functioning properly. A good deal of this work is performed before data is produced for later analysis. What is presented here are the checks made to post-production data.

The two detectors of greatest interest to this analysis are the TPC and the BEMC. The TPC is a mature and established detector at the STAR experiment, therefore much of the QA work for the TPC is performed prior to the data reaching the people doing data analysis. Furthermore the characteristics of the TPC were stable throughout the data taking. On the other hand, the BEMC is a new system, the bulk of which was installed directly prior to taking the data presented in this analysis. Therefore minimal pre-production QA was available for the BEMC, and more care must be given within this analysis. Additionally several BEMC hardware failures occurred over the course of data taking, altering the detector's configuration over the course of time. Extra care is given to account for these problems.

To begin the QA study of the TPC and BEMC, minimum-bias data, which reguires only a coincidence signal from the East and West BBC's, will be examined. Examining high tower data is more complicated particularly when doing QA work because the BEMC is strongly coupled to the trigger.

4.3.1 TPC

Tracks are charged particles reconstructed by the TPC. For minimum bias collision, the charged particle production is expected to be azimuthally symmetric about a collision and therefore uniform in phi. However, not all charged parti-

cles will be reconstructed. Any resulting non-uniformity in phi would indicate a non-uniformity in the detector. As can be seen in Figure 4.5 the ϕ uniformity is relatively good. It is not however perfect, depending on the momentum of the charged tracks, up to 10% of charged particles may fail to be reconstructed by the detector. These types of detector inefficiencies can be replicated by simulations and give no need for concern at this stage of the analysis. The eta distribution of tracks should also be approximately flat in this region of the detector, however TPC efficiency is strongly dependent on the track's η and falls off quickly around $|\eta| \approx 1$. The important point from a QA standpoint is that these efficiencies are constant throughout the data taking.

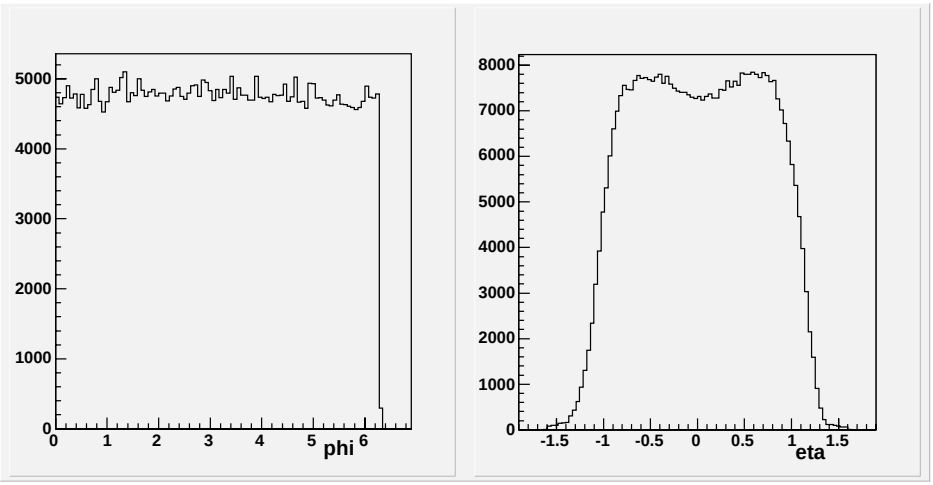

Figure 4.5: The left hand histogram depicts the azimuthal symmetry of reconstructed charged particles seen by the TPC in minimum-bias data, and on the right hand side the eta (η) distribution of charged tracks is shown. The tracking efficency of the TPC drops off sharply beyond $|\eta| > 1$.

For a given event the transverse momentum, $p_\perp$, of all reconstructed tracks in the event may be summed together. Figure 4.6 displays summed $p_\perp$ of all tracks for an event distribution as a probability distribution. The mean value of the summed $p_\perp$ is a convenient quantity for two reasons.

First the summed $p_\perp$ is sensitive to any number of problems which may occur. For example, if part of the detector would stop functioning, tracks in that region would not be reconstructed and the summed $p_\perp$ of the event would drop. Another example would be if multiple collisions were occurring during an event readout. In this case an excess of energy would be recorded by the detector.

Second, the summed $p_\perp$ is a very similar quantity to the jet's $p_\perp$, the quantity we are interested in measuring. The notable differences being that the reconstructed jet's $p_\perp$ includes both the BEMC and the TPC detectors, and that the energy must be localized.

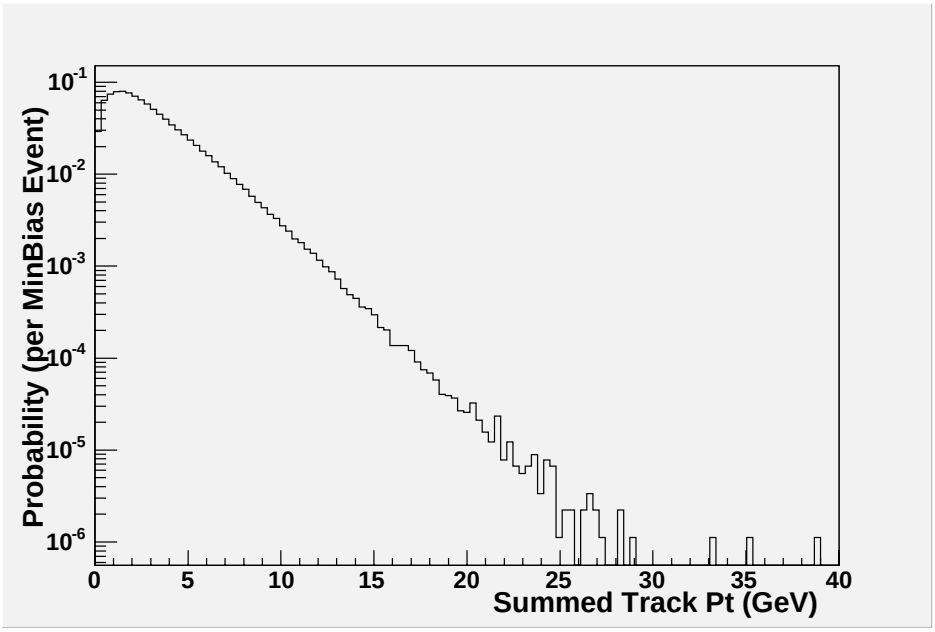

Figure 4.6: All tracks within an event are summed provided they fulfill a set of requirements. The requirements include a minimum $p_\perp$ of 0.2 GeV, $|\eta| < 1.6$, that the track pass within 2 cm of the collision point, and a minimum of 15 fit points, TPC pads above a nominal threshold, used to reconstruct the track. These criteria are very standard within the STAR collaboration and are used repeatedly throughout the analysis.

In Figure 4.7 the average summed track $p_\perp$ of the event is time-ordered to better locate anomalies that may occur during the entire data taking period.

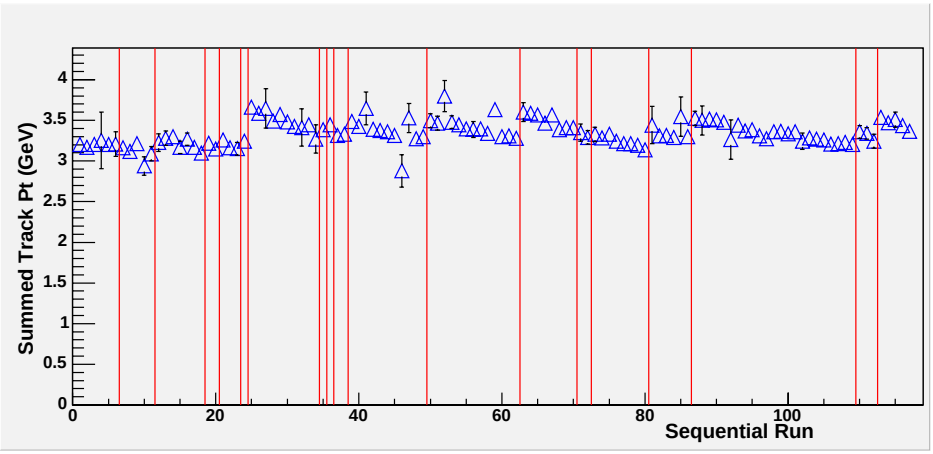

Figure 4.7: The data is subdivided by run number. The vertical lines denote when stored beams where dumped and replaced by new beams in the RHIC collider. Pile-up appears to occur at the beginning of the stores.

The most notable feature is the enhanced total energy found at the beginning of beam stores. The explanation for this type of enhancement is that multiple collisions are occurring within a single readout of the TPC electronics. These additional collisions are called *pile-up*. When the beam is initially injected more protons are stored and more collisions occur. With time the beam deteriorates and fewer collisions occur. With fewer collisions, the probability that multiple events will occur at both the same location and within the same time window as the electronics readout falls.

Although this problem is noted, it is not severe enough to warrant action at this time. The *pile-up* only contributes up to an additional 10% of summed transverse energy to the minimum-bias event as shown in Figure 4.7 near run 25. If this energy is randomly distributed over the entire TPC volume, as expected, the additional energy has little influence over the localized measurement of the jet. Specifically, the additional 0.3 GeV of energy would be distributed approximately uniformly over 2 units in η, [-1,1], and 2π in ϕ covering a total of area 4π. A measured jet only samples $\pi r^2 = \pi(0.4)^2$ of the area. The jet's area is therefore

only 4% of the total area, so we would expect appoximately 0.012 GeV of energy from *pile-up* to contribute to the jet. In the future this effect will become more important because collision rates are expected to increase by as much as ten times the 2003 rate.

4.3.2 BEMC

The 2003 was a successful year for the BEMC: a substantial portaion of the detector, optics and electronics were installed, the BEMC was added into the triggering system, and data was recorded for the entire running period. That said, commissioning the BEMC was a more arduous task than monitoring the stability of the TPC.

The most basic assessment of the system is its active detection region. Particularly in the case of reconstructing large and composite objects such as jets, large and continuous areas of detection are needed. The large acceptance of both the TPC and BEMC make these detectors well suited for the task of jet reconstruction. Although the TPC was very stable over the 2003 running period, the BEMC did encounter a string of electronics failures. The failures stemmed from a diodes in the electronics crates sensitive to the magnetic field.

There are fifteen electronics crates, and each crate services 160 individual channels (towers) of the detector, covering a slice of the detector 1 unit in $\Delta\eta$ and $\frac{2\pi}{15}$ radians in $\Delta\phi$. Failures appeared to occur at random positions in ϕ. When replacements were not available, working crates were swapped around the detector to maintaining one continuous active region and a single inactive region.

There were failures of individual towers as well. Some towers were screened out during the data taking period as soon as the towers looked problematic. The quality of additional towers was called into question after data taking, and their

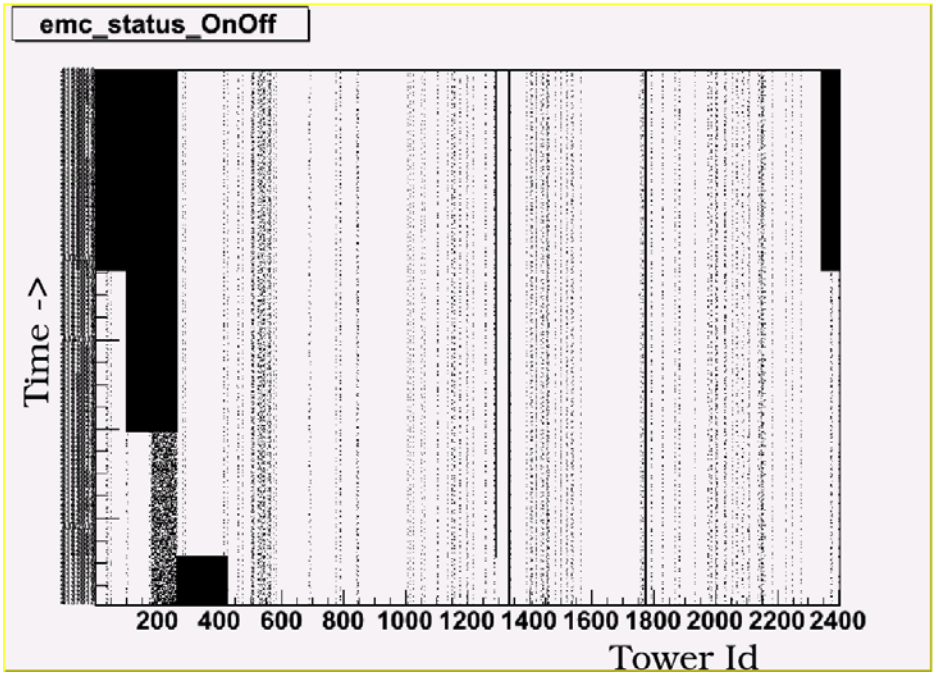

Figure 4.8: The status of the BEMC's 2400 towers are plotted above. The white section indicates active towers used in the data. The black markings indicate towers that were either inactive during the run or deemed faulty after data taking commenced. The y-axis denotes each run, but can roughly be construed as time. Often towers straddled the line of usable and unusable, as seen by the dotted vertical lines. These towers are all completely removed in the analysis. Finally the electronics crate failures are clearly seen as they occur over the two week period.

output was discarded. Several criteria were used to check the status of each tower and the quality of its output. The most common reasons to discard data was either a noisy or an under-active tower response. Examples of under-active tower responses include broken optical fibers and failures in the PMT high voltage power supply. Many of the overactive towers were also attributed to malfunctions in high voltage supply, as well as stuck bits in readout electronics. A complete summary of towers deemed admissible to the analysis is shown in Figures 4.8. A summary of overview of the active towers used in the analysis is shown in Figures 4.9 and 4.10. The η and ϕ regions active can be seen. In particular the missing acceptance in phi from the electronics failures is clearly visible in Figure 4.9.

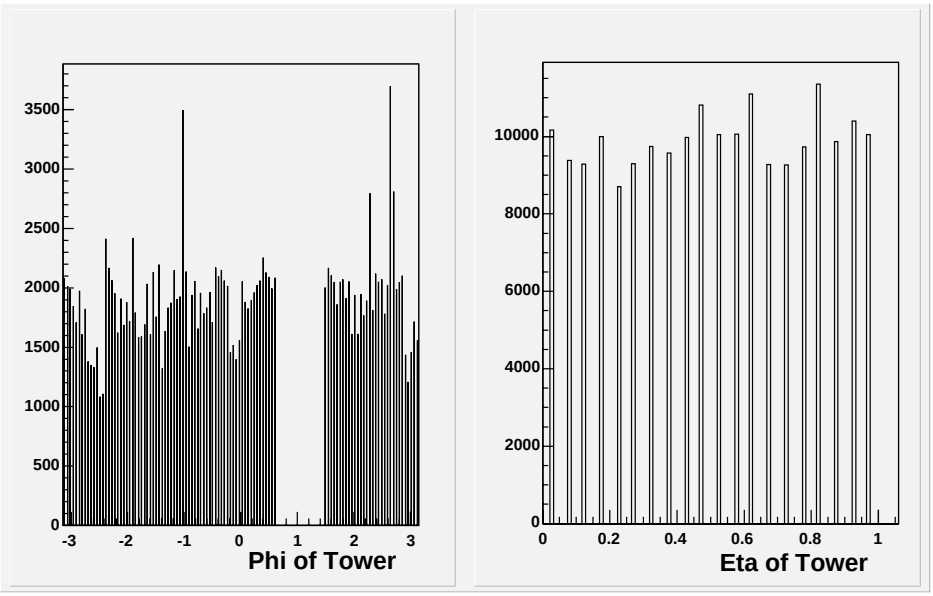

Figure 4.9: Similar to Figure 4.5, the left and right hand histogram depict the ϕ and η distributions of towers recording over 0.2 GeV of transverse energy. The data shown is all minimum bias events taken on day 150 (the last day data was recorded in 2003). The hole from the broken electronics crate can be seen in the azimuthal distribution.

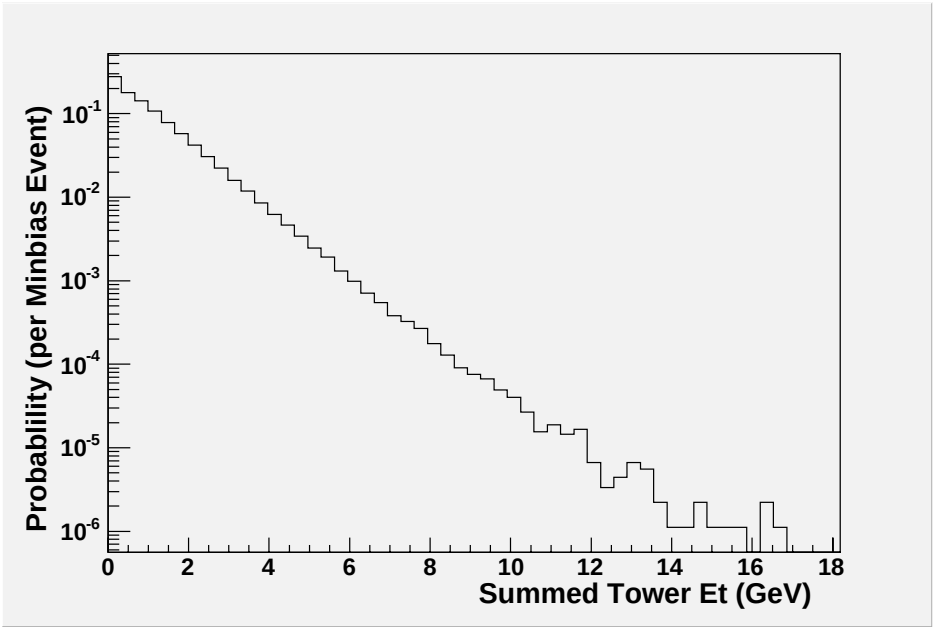

Figure 4.10: The transverse energy of all towers are summed for each event and plotted above. Only towers with greater than 0.2 GeV of transverse energy are considered.

4.4 Beam Background

All experiments are susceptible to backgrounds of various sorts. In the case of the STAR detector, the beams are steered to collide at the center of the detector, and STAR is built expecting all particles to come from this collision. Possible contaminations to these collision may occur from cosmic rays, beam-gas interactions, or other beam related backgrounds. In practice the largest source of background came from the latter, an upstream beam-related background source from an undetermined location. Figure 4.11 provides a schematic of this source.

The bulk of particles from the upstream background source traversed the STAR detector unnoticed in either the TPC and BEMC. This is partly because the TPC and the TPC's tracking code are specifically designed to be used on particles originating from the collision region - not from outside of the detector.

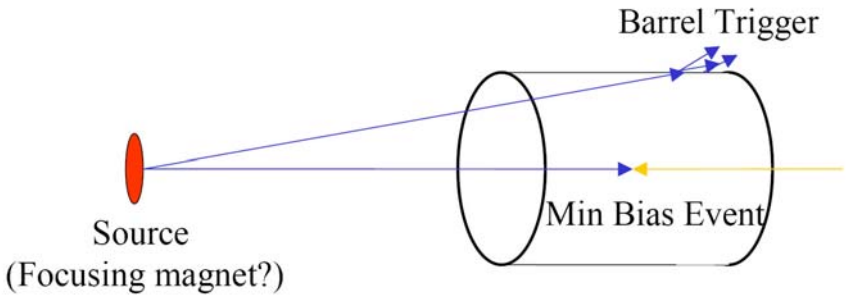

Figure 4.11: Two beam bunches enter the detector simultaneously from the East and West. A portion of the East beam then deviates off course, traversing the detector instead of passing through the collision region. The remaining East beam enters the collision region, often colliding with the West beam bunch. The collision's information and the traversing West beam's information are there unintentionally merged and recorded into a single event. Usually these merged events are easily removed from the data.

Alternatively, the BEMC was responsive to the background particles entering into its towers, but lacked the tracking capacity necessary to discern their origin. In general the BEMC must rely on the tacit assumption that all observed particle originate from the triggered collision unless proven otherwise. In truth, the problem may have continued unnoticed if the deposited energies from the background into the BEMC were not so large to have rivaled the jet's signal.

STAR is designed to filter out erroneous data that may occur from beam backgrounds or cosmic rays. The filtering process begins at the triggering system, specifically with the BBC. For data acquisition to begin, scintillators from both the East and West BBC detectors must fire within a time window indicative of a collision. To discriminate if the signals were from a collision of beam background, the timing of the East and West BBC signals are compared. If the East signal follows the West signal by a time comparable to a particle passing through the East and then West at the speed of light, or vice versa, the event is considered to occur from background. The collision and background signals are compared

and used as an indicator of the quality of the beam.

Non-trigger detectors are also used to filter out background. From the TPC, only tracks pointing to the reconstructed collision vertex are used in the analysis. This minimizes the cosmic ray background entering into the data. This method also helps to filters out pile-up events and beam background in the TPC. Although the BEMC cannot discern a particle's origin, it can be used to discriminate collision-signal from background by using a narrow timing window.

The upstream background was most prevalently found in the high tower triggered data set. Background particles created electromagnetic showers horizontally across the detector, satisfying the trigger's energy requirements. Simultaneously the minimum bias trigger must have be fired with real events - most often real events that would not have otherwise satisfied the high tower trigger's requirement.

Because the BBC was not able to screen out all of the background, software cuts must be applied in the analysis to screen the data. As mentioned the BEMC can not discern the origin of measured particles, so to remove events with background present a coincidence of energy is required from the TPC. Fortunately, checking for this coincidence can be done by applying the same tools as used to find jets used in the analysis.

4.5 Jet Finding

To first approximations, a jet is an ensemble of particles all originating from a single scattered parton. By re-esembling the jet from the detected particles an understanding of the original parton's momentum can be obtained. Several techniques have been developed to find and reconstruct jets. The one implemented in

this analysis is a mid-point cone algorithm adapted from the CDF collaboration.

A handful of variables are often employed to describe reconstructed jets. One of note is the jet's radius, which is based off the two Lorentz invariant quantities η and ϕ.

$$R = \sqrt{\eta^2 + \phi^2} \tag{4.1}$$

The four momentum of the jet is also useful, and defined as

$$p_\mu^{jet} = \sum p_\mu^{particles} \tag{4.2}$$

Jet identification is a relatively straightforward proceedure. Within an event all TPC tracks and BEMC tower responses, *hits*, above a threshold of 200 MeV are recorded along with their kinematic variables. These tracks and hits are then assorted into a grid of η and ϕ bins. Often times, more than a single track or hit is pointed into an η/ϕ bin. In these cases the multiple four-momemta of the particles are added together as described in equation 4.2.

One important issue to consider when employing this type of algorithm is the possible double counting of charged particles that also deposit energy into the BEMC. To correct for the double counting of anergy from these particles, TPC tracks are extrapolated to BEMC tower and the energies are checked. If the struck tower is found to contain energy, one MIP's worth of energy - the most probable amount of energy deposited by a hadron - is subtracted from the bin. This amount subtracted varies from approximately 250 to 350 MeV, depending upon the η location of the tower. Towers at higher η tend to have larger amounts of energy deposited into them from charged particles.

The bins containing the track and hit energies are now sorted by energy. The

most energetic bin is chosen first, and all bins within the prescribed jet radius are associated with the seed bin. This possible jet is labeled a *proto-jet*. In this analysis the radius was chosen to be 0.4, the minumum seed energy to be 500 MeV, and the minimum associated bin energy to be 200 MeV. The procedure is repeated with all bins above the seed threshold, creating a list of proto-jets. The midpoints between each of the seeds are also used as seeds and added to the list of proto-jets.

With the complete list of proto-jets is finished, the proto-jets are are all compared to one another to see if overlaps exist. Proto-jets above 5 GeV that do not overlap with other proto-jets are promptly promoted to jet status. Overlapping proto-jets may either be merged into a single jet or split into two adjoining jets each sharing some portion of the overlapping energy. Proto-jets sharing 50% or more of their energy are merged, those sharing less than this amount are split. In the case of split jets, the shared bins are divided such that the shared bins are assigned to the nearest proto-jet.

4.6 Cuts Applied to Reconstructed Jets

The completed list of jets is now subject to a series of finalizing cuts. The cuts fall into a handful of categories and are shown in Figure 4.12.

- Fiducial cuts on the jet center's position.
  - $0.2 < \eta < 0.8$
  - $|\phi - 1.3| > 0.75$
- Location of the collision within the detector.
  - |collision z-vertex| < 0.75

- Cuts to remove beam background from the data set.
  - $\frac{E_{\perp}^{neutral}}{E_{\perp}^{total}} < 0.8$
  - Jet TPC $P_{\perp} > 1.5$ GeV
- A software re-application of the high trigger.
  - Tower Trigger $E_{\perp} > 3.5$ GeV

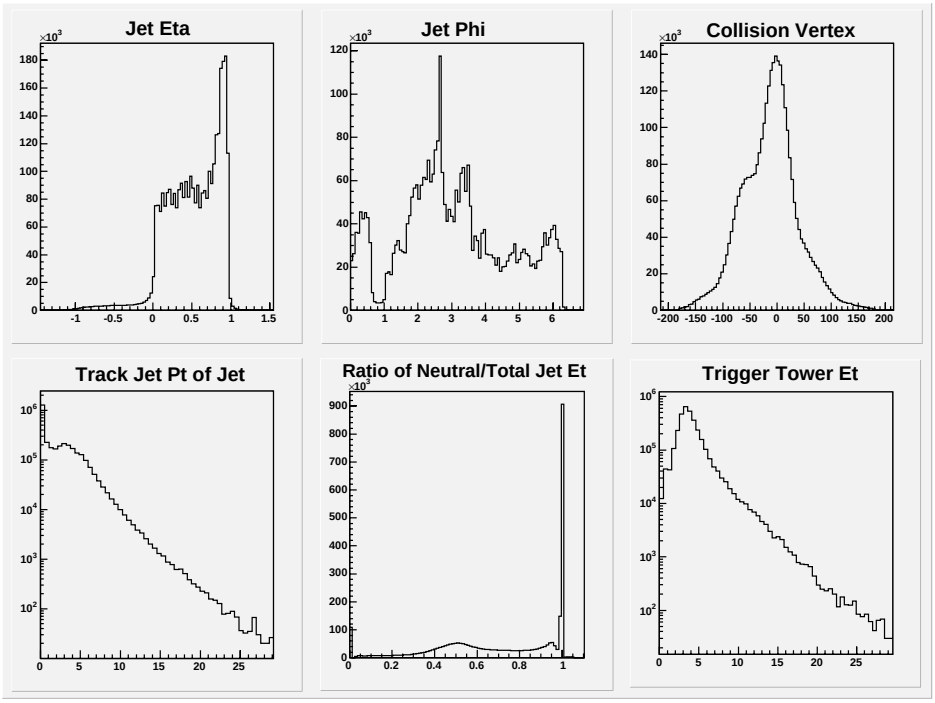

Figure 4.12: The above distributions display the quantities subject to cuts. The jet's η and ϕ distributinos are not flat and uniform as expected. The excesses are primarily attributed to the beam background striking the detector. Electronics failures in the BEMC are responsible for the hole seen in the phi distribution and located near $\phi = 1$. The bottom middle plot most clearly illustrates the beam background. The sharp spike representing neutral energy not associated with charged TPC energy clearly sepatates usable data from background contamination.

The fiducial cuts on the η and ϕ position of the jet's center are used to ensure the jet falls within the active portion of the detector by a margin of 0.2 in η-

ϕ space. Specifically these are $0.2 < \eta < 0.8$ and $|\phi - 1.3| < 0.75$. The ϕ cut is made to omit the region where crate failures occured. The 0.2 margin would ideally be 0.4, the defined radius of the jet, however this greatly reduces the statistical percision of the measurement, while only modestly improving the energy resolution of the reconstructed jet.

The previously used cut on the collision vertex is maintained, such that collisions occur within 75 cm of STAR's center. Once again, STAR is ideally suited to examine data at the center of the detector, with greater statistics this cut may be re-examined and possibly reduced.

Cuts to discern the faux jets caused by beam background from the jets created in the collision region are based on a coincidence between the TPC and BEMC. All jets containing less than 1.5 GeV of TPC $p_\perp$ or with less than 20% of their total $E_\perp$ coming from the TPC are removed from the analysis. These background-jets, which we would like to remove from the data sample, have preferred η and ϕ locations. This can indirectly be observed in Figure 4.12.

Lastly, the re-application of the high tower-trigger is done for two specific reasons. The first is to remove data from towers originally in the trigger but later deemed unstable or unusable. The second that the hardware triggers were not precisely set at their nominal value 3.5 GeV. This cut removes data taken from good towers calibrated below 3.5 GeV using the most precise calibrations available.

4.7 Final Data

The cuts employed do a reasonably good job of cleaning up the data. The results in Figure 4.13 display the basic distributions as seen in Figure 4.12, now with

the cuts listed above applied. The strong η dependence is no longer seen from the beam background, leaving only the periodic markings of the calorimeters towers. The trigger condition of a single tower containing greater than 3.5 GeV of energy strongly biases the results as can be seen in the periodic structure of the η distribution. The ϕ variation is largely attributed to the working geometry of the calorimeter, but a small amount of background appears to persist in the data. This can also be seen in the bottom middle figure.

With the cuts in place, the data is in a position to be analyzed. Results in the following chapters rely on the data as described using the cuts and selections discussed above. The spin dependent quantities, A_L and A_{LL}, make additional selections on runs not necessary in the analysis of the inclusive cross-section. The final runs used in the asymmetry analysis will additionally require a measured and non-zero polarization, and must also contain information on the relative luminosities of the beam's different spin orientations. These will be discussed in further detail in the following chapter.

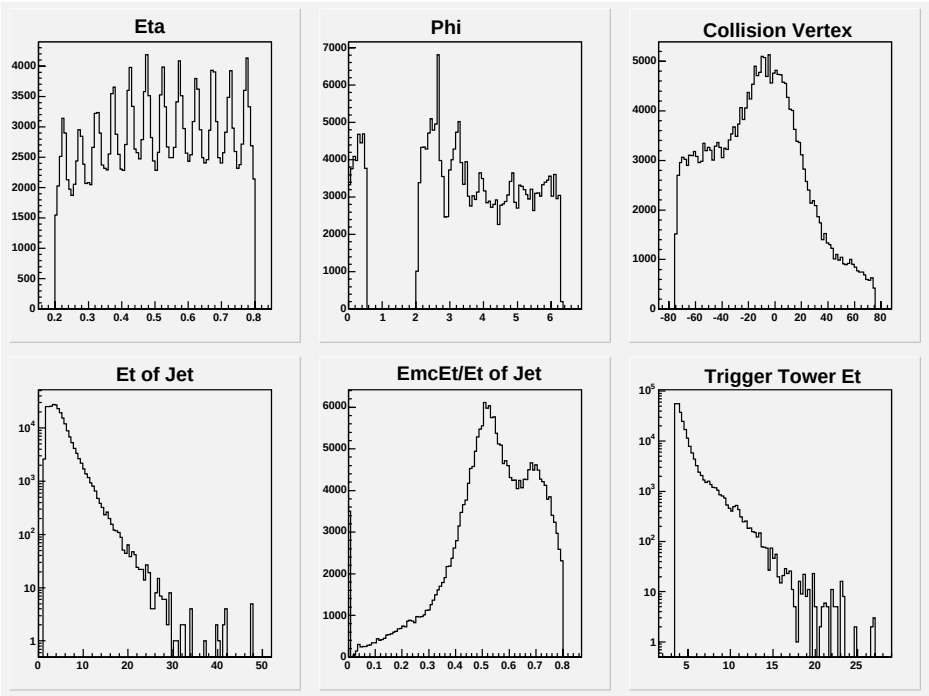

Figure 4.13: The data, post cuts, as used in the analysis.

CHAPTER 5

Analysis

Two of the most fundamental and intriguing measurements we can perform using the jets from data collected at STAR are the inclusive jet cross-section and the double-spin longitudinal asymmetry, A_{LL}. A_{LL} is of particular interest because it is expected to be sensitive to the gluon's polarization. However any comparison drawn between the results from the data and the theoretical expectations put forth from pQCD requires the assumption that pQCD is valid in the kinematic region measured by the experiment. The inclusive cross-section is a particularly good candidate to test this assumption because it is both insensitive to the gluon's polarization and well determined by both theory and experiment. If the inclusive cross section predicted by theory agrees with those measured by experiment, then we can feel relatively confident that a comparison of the longitudinal asymmetries may also be made between the theory and experiment.

5.1 Inclusive Cross-Section

To characterize how often a certain interaction will occur, in this case a jet produced in the STAR detection region, it is customary to define an effective size of the nucleus or particle for the particular reaction of interest. This characteristic is called a cross-section. At the most basic level, the cross-section, σ, is defined by

$$N = \sigma * I \tag{5.1}$$

where N is the number of jets, σ is the jet's cross-section, and I is the number of proton-proton interactions. The more common employed differential cross-section for particle production is found by counting the number of particles, d^3n, produced in a phase space element, and expressed in an Lorentz invariant form.

$$\frac{d^3\sigma(p_\perp)}{p_\perp d\eta d\phi dp_\perp} = \overbrace{\frac{d^3n(p_\perp)}{p_\perp d\eta d\phi dp_\perp}\underbrace{\frac{\sigma_{BBC}}{N_{MB}}}_{1/I}}^{\sigma=n/I} \tag{5.2}$$

5.1.1 Determining I, the Number of Proton-Proton Interactions

The BBC keeps track of the number of total number of proton-proton interactions that occur during the running period. To do this, a separate measurement must be made to determine the beam's luminosity, $\mathcal{L}$, which is the time derivative of the number of interactions.

The beam luminosity can be determined through the relation given in Equation 1.4, found in the introductory chapter. The variables in equation 1.4 are all monitored during the running with the exception of $A_{overlap}$, which is the overlap area of the two beams. This value can be determined by performing a Vernier scan that measures the profile of the beams.

At the time of the Vernier scan, the BBC counts the number of minimum bias events (satisfying the standard minimum bias coincidence condition) that occur. Then using the concept of Equation 5.1, the BBC's cross-section, σ_{BBC}, can be determined and is measured to be $26.1 \pm 0.2(stat) \pm 1.8(syst)$ mbarns [Ada03].

Thus STAR can use the BBC to determine the luminosity, i.e. the number

of proton-proton interactions, at any given time by counting the number of minimum bias collisions that occur in that time interval. The number of minimum bias events is then mapped back to the total number of proton-proton collisions through σ_{BBC}.

In practice determining the number of minumum bias events used in the jet analysis is relatively straight forward though not trivial. STAR does not record every minimum bias event, but instead records a representative sample. Each data run has its own pre-scale factor that determines what fraction of the minimum bias events are recorded. If the pre-scale factor is set to 4000, then every 4000th minbias event is saved, and the other 3999 are discarded. So the total number of minbias events that occur in a given STAR run is simply the number of recorded minimum bias events in a run multiplied by the run's pre-scale factor.

The jet analysis does not however use the full beam luminosity. Recalling Figures 4.1 and 4.2, a restriction is placed on the collision's location, such that only proton collisions with vertices reconstructed by the TPC within 75 cm of STAR's center are used. Therefore the number of interest is not the total number of minimum bias events, but the number of minimum bias events occuring within 75 cm that may or may not have a reconstructed collision vertex.

Because the TPC can not always reconstruct a collision vertex, a correction must be made to the number of minimum bias events counted within 75 cm. We assume that the unreconstructed vertices follow the same shape as the reconstructed vertices. Then a single multiplicative normalization can be applied. From examining the data taken on the last day, 92,532 minimum bias events had reconstructed vertices out of the 104,975 minimum bias events recorded. From this we can determine that 89% of minimum bias events have a reconstructed vertex, therefore we must scale the number of events with found vertices by 1.123

to account for the lost events.

5.1.2 Determining n, the Number of Jets

We must now determine n, the number of jets in a given phase-space element. n is not necessarily the number of jets reconstructed by the detector, however n can be related to the number of reconstructed jets, N_0, through some correction factor, ϵ, that must be determined for each bin examined.

$$n = \frac{N_0}{\epsilon} \tag{5.3}$$

Two simulation packages, Pythia and Geant, are used in conjunction to determine these correction factors. The first package, Pythia [Sjo], is an event generator, and is well established, incorporating many results from prior experiments. Pythia emulates unpolarized proton-proton collisions and creates a list of particles, their momentum, and direction. This list is fed into a GEANT, a package used to simulate the STAR detector. A considerable amount of effort by many members of the STAR collaboration went toward correctly simulating the STAR geometry and response. Figure 5.2 depicts the geometry used by Geant to model the STAR detector. The detector's response to each particle is tabulated within Geant and passed to the reconstruction software.

The correction factor, ϵ, is determined by taking the ratio of the number of jets reconstructed by the simulated detector to the total number of jets entering a region of phase space covering the detector. To determine the number of jets entering the detection region, the list of particles generated by Pythia is entered into the jet reconstruction software. The same algorithm that is applied to the data is applied to the list of simulated particles producing the Pythia jets used

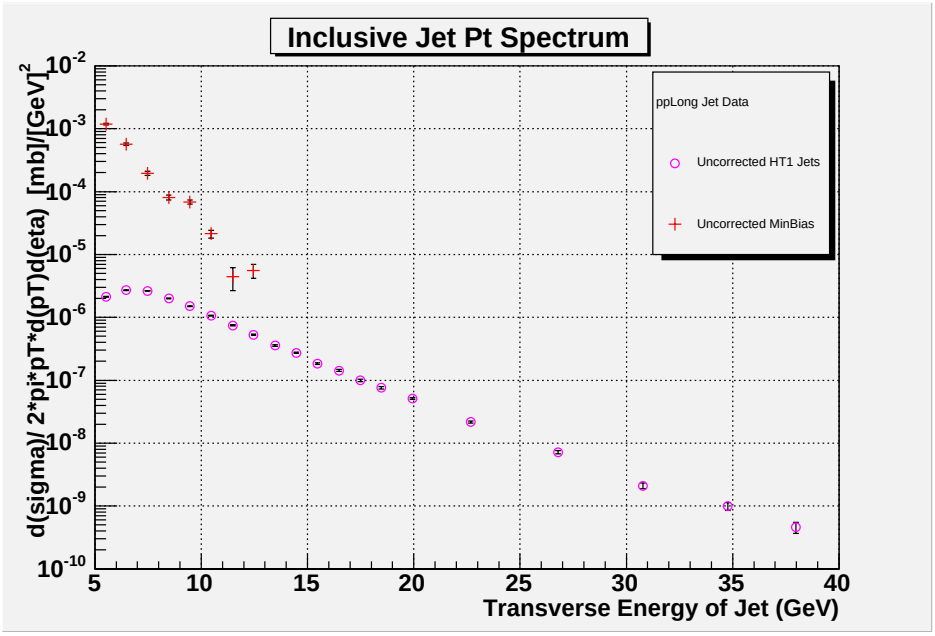

Figure 5.1: The uncorrected inclusive jet cross sections of the two data sets, minimum bias and high tower, are shown above. Without the corrections applied from simulations, the two data sets are distinctly separate. Accounting for this inefficiency, or bias, is the primary purpose of the simulations.

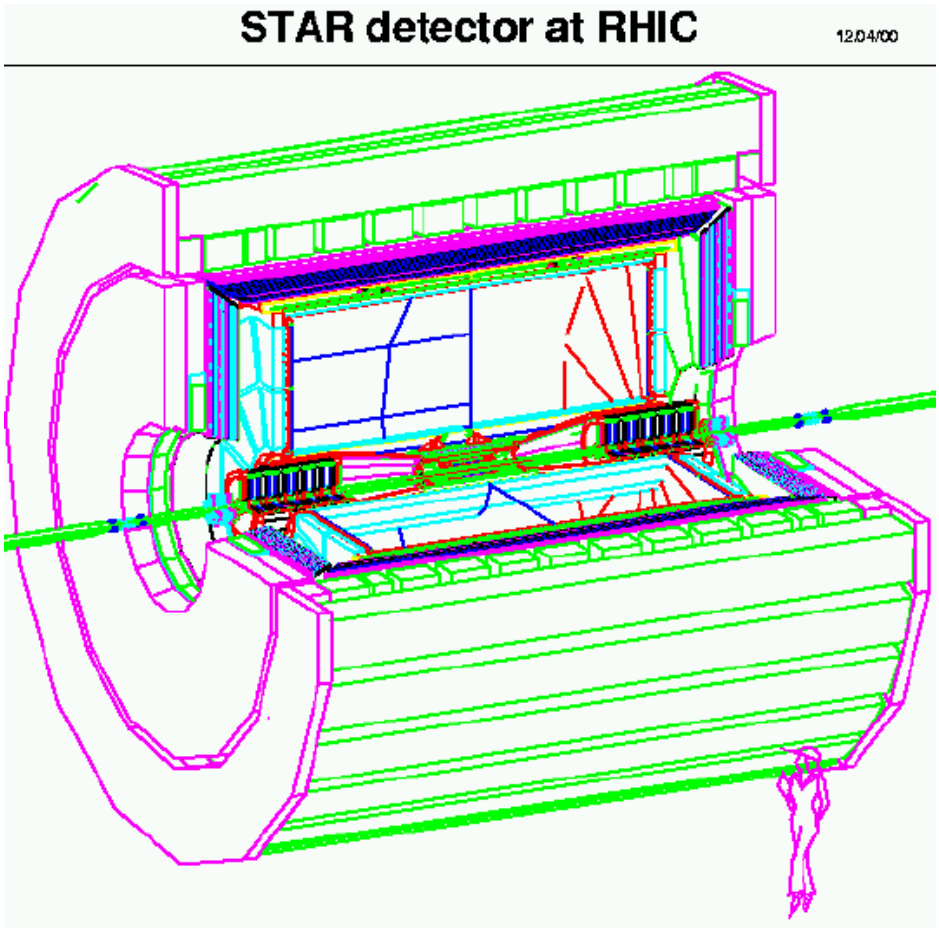

Figure 5.2: A visual representation of the STAR detector created in Geant. Events simulated by Pythia are fed into this detector simulator to understand the detectors response. Although only two detectors, the TPC and BEMC, are directly used in the analysis, the materials from other detectors, support structures, and the beam pipe all influence the measurement. The outer most shell shown is the return yoke used to moderate the magnet's flux.

in the denominator.

The numerator, the number of jets reconstructed by the simulated detector, is found using Geant's output. The list of simulated TPC tracks and EMC towers from Geant are fed into the jet reconstruction algorithm, and the reproduced jets are subject to the same cuts used by the data. This includes the high tower trigger condition of 3.5 GeV of transverse energy in a single tower.

One important note is that the jets reconstructed using the Pythia output will not have precisely the same energy as the leading parton (quark or gluon) they stem from. Once fragmentation occurs some of the outgoing jet can leave the reconstructed cone region, leaving the jet with less energy than the original parton. Conversely unrelated particles may enter the cone region of the jet increasing its energy beyond that of the original parton. Because of these factors we do not measure parton energies, only jet energies.

In a like manner, the energy of the jets reconstructed by the STAR detector have the potential to stray even further from the original parton's energy. Geant is used to mimic the detector inefficiencies and overcompensations. Particles such as neutrons are not charged and therefore will not be detected by the TPC. Likewise because neutrons are hadrons (heavy), they are unlikely to deposit a significant portion of their energy into the BEMC. Geant is responsible for taking all of these detector effects into account.

$$\epsilon = \frac{n_{jets}^{Geant}}{n_{jets}^{Pythia}} \tag{5.4}$$

The raw yields, uncorrected by simulations, are shown in Figure 5.1. The high $p_\perp$ region of the jet yield is exponentially declining as would be expected. The low $p_\perp$ region does not follow this expected pattern, and the reason is the because

of the high tower trigger. Jets in the lower $p_\perp$ region are unlikely to deposit the required 3.5 GeV of transverse energy into a single EMC tower necessary to fire the trigger and record the event.

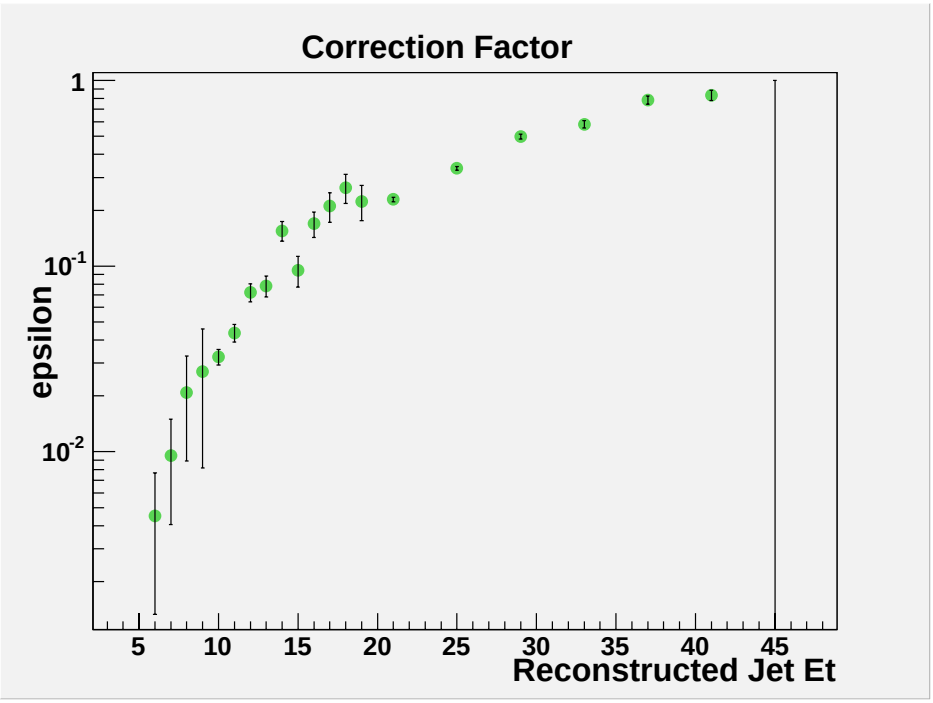

Figure 5.3: The correction factor, ϵ, that is applied to each bin of inclusive cross section ranges across two orders of magnitude. Three sets of simulations are used to obtain these factors. The statistical precision of the lowest $p_\perp$ sample is the poorest, whereas the highest $p_\perp$ region is the best understood.

The effects of this trigger requirement can also be seen in Figure 5.3. Figure 5.3 graphs the correction factors across the range of reconstructed jet $p_\perp$ examined in this analysis. High $p_\perp$ jets entering the detector are more likely to be reconstructed than lower $p_\perp$ jets because of the scale difference between the reconstructed jet energy and the trigger energy.

At the largest bins, the correction factor approaches 1. Although 100% correction efficiency could be interpreted as perfect jet reconstruction, a second effect called *feeddown* arises from the detector's imperfect resolution and the

spectrum's shape. The smearing from the resolution artificially flattens the $p_\perp$ spectrum.

This effect is significant because the jet spectrum is exponentially decreasing in $p_\perp$. Therefore jets promoted into higher $p_\perp$ bins, which have considerably smaller populations of jets, are more noticeable than jets demoted into lower $p_\perp$ bins, which have substantially larger jet populations.

One piece of information not included in the simulations was the BBC trigger condition. This correction must be applied separately. Prior studies [Ada03] of the BBC's response in proton-proton collisions indicate a constant efficiency of 0.79 ± 0.18 across the $p_\perp$ region examined. All ϵ's expressed in Figure 5.3 are multiplied by this number in the analysis.

5.1.3 Estimate of Background Contamination

In Chapter 4 we discussed backgrounds that could effect the analysis results. The largest source of background came from the beam upstream of the detector. The postulate was that prior to entering the collision region beam would veer off course, most likely because of focusing or aligning magnets near the STAR detector. This stray beam would spray across the detector, depositing energy into the barrel electromagnetic calorimeter. This would happen in coincidence with "good" beam that was colliding in the interaction region and satisfying the minimum bias trigger. Because the BEMC does not have tracking information, the contaminating particles are not easily discerned from particles created by the proton-proton collisions in the STAR interaction region.

Since the BEMC is unable to efficiently and reliably screen the background on its own, a conicidence condition was imposed on the jets post analysis. All jets must meet two additional criteria: at least 1.5 GeV of the jet's transverse

momentum and over 20% of the jet's transverse momentum must be measured by the TPC. In principle and practice these cuts are very similar. The 1.5 GeV cut places slightly stronger constraints on low energy jets, while the ratio cut is more a stringent cut for the higher energy jets.

Even after these conditions were imposed some background remained. For example, a 5 GeV jet may couple with 5 GeV of background energy and be measured as a 10 GeV jet. We can attempt to estimate this contribution from the background by comparing data taken at different times, because the background was larger during high luminosities and smaller at low luminosities.

The neutral energy fraction, $\frac{E_T^{BEMC}}{E_T^{BEMC}+E_T^{TPC}}$ for high and low luminosity jets can be normalized by the number of minimum bias events as described above. The difference in the normalized spectra is the shape of the beam background. However because background may be present in the low luminosity sample, the absolute size of the background can not be determined solely from the data.

To normalize the background simulations are used. Simulations predict that approximately 10% of measured jets should have an neutral energy fraction equal to 1. The background shape is normalized such that the neutral energy fraction greater than 0.95 is 10% of the total data sample. The background shape is then subtracted from the uncorrected data. The normalized background, un-corrected data, and difference of the two are shown in Figure 5.4.

To estimate the contamination by the background, we simply integrate over the region used in the analysis, energy ratio less than 0.8, for both the data and estimated background contamination. The correction to the data is found to be approximately 7.5% $\pm$ 2% for all $p_\perp$ bins. Therefore a 7.5% reduction to the overall cross section is applied to the final results.

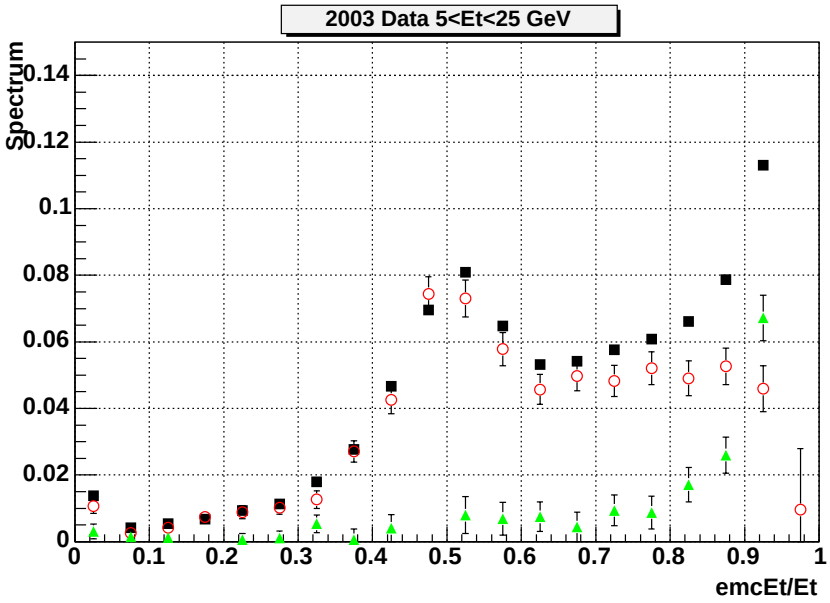

Figure 5.4: Plotted from highest to lowest: all data (squares), all data minus background contribution (circles), and estimate of background contribution (triangles). The x-axis is the ratio of neutral to total energy of the measured jet - this quantity sensitive to the beam background. The background contamination is estimated to be $7.5\% \pm 2\%$ at all jet energies.

5.1.4 Systematic Errors on the Inclusive Cross Section

The measurement of the inclusive jet cross section is limited by systematic errors at mid to high energies. At low energies poor statistics from simulations rival the systematics in the understanding of the jet cross section. From Equation 5.2, three terms contribute substantially to the jet cross section: n, σ_{BBC}, and N_{MB}.

The total number of minimum bias events, N_{MB}, is well understood. Millions of minimum bias events are observed during each run, therefore the statistical error from this number is quite close to zero. The pre-scaling of the minimum bias events limits the resolution of our understanding. This is because the total count of events may be off by as much as $\pm$ the pre-scale factor before incrementing the next minimum bias event. This error is therefore the fraction, $\frac{1}{n_{MB}}$, where n_{MB} is the number minbias events recorded by STAR. From Tables 5.1 through 5.4, the number of recorded minimum bias events is always greater than 200, and often several thousand. Therefore this error is negligible.

The BBC's cross section is measured to be $26.1 \pm 0.2 \pm 1.8$, an 8% overall uncertainty to the measurement, which must be propogated to the jet analysis. A larger uncertainty comes from the correction applied to the triggering efficiency by the BBC. The trigger efficiency may range from $0.61-0.97$ [Ada03], corresponding to a 31% shift upward or 20% shift downward overall uncertainty.

Finally the number of jets reconstructed by STAR may be incorrect. The BEMC is of greatest concern. If miscalibrated too high or too low, the overall number of jets reconstructed could vary greatly. In practive though this number is not overwhelming. The BEMC is calibrated by two different analyses. A tower by tower calibration is done using charged hadrons and an overall normalization to the BEMC is determined through electrons. The overall uncertainty in the electron calibration is 3% [Sua1]. When the 3% calibration error is propogated

through the analysis the result is an 8% error to the jet cross section. A more conservative approach is to use the difference, 6%, between the results of the charged hadroni [Sua2] and electron calibrations [Sua1]. A 6% shift in BEMC energies corresponds to an 18% shift in the overall jet cross section.

In all, the systematic errors on the jet analysis are larger than the statistical errors. The dominant error is the uncertainty in the BBC's triggering efficiency for the high $p_\perp$ jets which is currently under further investigation and should be improved upon soon. The uncertainty from the BEMC's energy scale and the cross section of the BBC will ultimately be the limiting factors of the measurement.

5.1.5 Inclusive Jet Cross Section Results

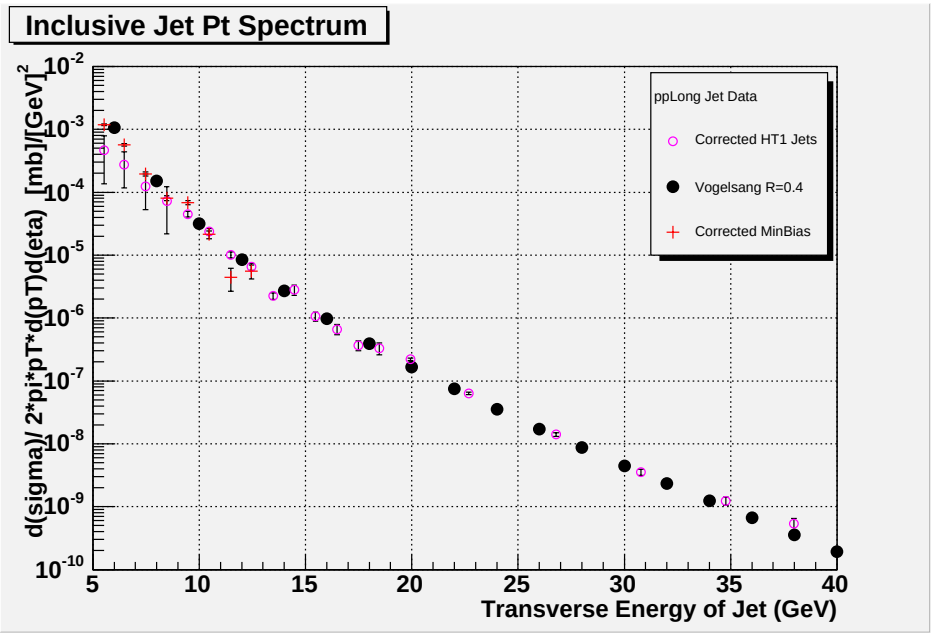

Figure 5.5: The inclusive jet cross section for data from minbias and high tower triggered data. Data from the high tower trigger sample measures jets comfortably past 30 GeV of transverse energy.

Once the correction factors are applied to the measured spectrum, we arrive at the final cross sections which are presented in Figure 5.5. Notice that the two data sets, minimum bias and high tower triggered, overlap once the corrections are applied. The statistical precision is poorest for lowest bins because of limited simulations, here additional simulations are underway that will improve the understanding of this region.

Finally we can compare the measured results with theoretical expectation. The calculations are generated from code written and developed by Werner Vogelsang. The calculations utilize the CTEQ-6 parton distribution functions, and include both LO and NLO contributions. Special care was taken to match bin sizes and fiducial volumes between the calculations and the experimental setup. In Figure 5.6 the ratio of (Data - Theory)/Data is displayed. Errors shown are statistical and include only uncertainties from the data and simulations.

For the leftmost points seen in Figure 5.6, the data appears systematically smaller than theory. This may possibly be explained by an unphysical cutoff used in the Pythia simulations. All contributions from partons under 3 GeV were neglected in the simulations, however some of these lower $p_\perp$ partons may well *feeddown* into the 5-6, 6-7, and 7-8 GeV bins in the data, but remain unaccounted for by the correction factor. Nonetheless, the differences are within a one sigma statistical variation from zero so no real conclusions can be drawn.

5.2 Asymmetries

The longitudinal asymmetries are found by comparing the cross sections of differing helicities. Proton bunches that have their magnetic moments aligned with their incident direction have a positive helicity, +. Similarly proton bunches with

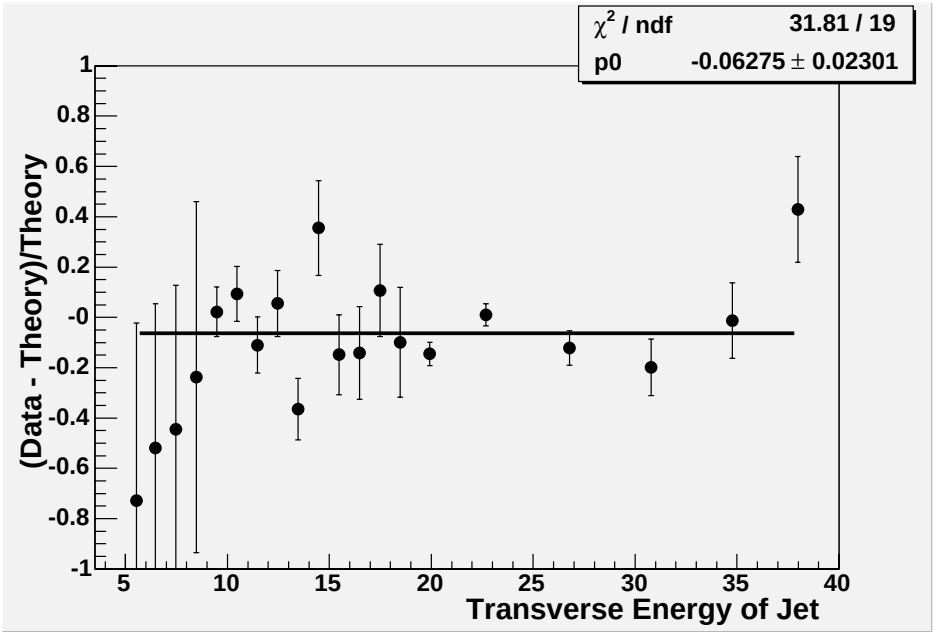

Figure 5.6: Comparison of measured inclusive jet cross section with theoretical NLO pQCD calculations. In general the agreement between STAR results and NLO pQCD calculations are good. The systematic errors, which may be as large as $\pm 30\%$, namely from the BBC's overall normalizaton are not shown.

spins anti-aligned with the beam direction have a negative helicity, $-$. Four possible combinations of longitudinally polarized proton-proton collisions are possible: $++$, $+-$, $-+$, and $--$. From these combinations, the single spin and double spin longitudinal asymmetries are written as

$$\begin{aligned} A_L &= \frac{1}{p}\frac{(\sigma_{++}+\sigma_{+-}) \;-\; (\sigma_{-+}+\sigma_{--})}{(\sigma_{++}+\sigma_{+-}) \;+\; (\sigma_{-+}+\sigma_{--})} \\ A_{LL} &= \frac{1}{p_1 * p_2}\frac{(\sigma_{++}+\sigma_{--}) \;-\; (\sigma_{+-}+\sigma_{-+})}{(\sigma_{++}+\sigma_{--}) \;+\; (\sigma_{+-}+\sigma_{-+})} \end{aligned} \tag{5.5}$$

where the p's are the beam polarizations, shown in Figure 5.7. Recalling equations 5.2 and 5.3, we see that most of the factors within the cross sections are identical regardless of their helicity state. These common terms can be factored out of the numerator and denominator to cancel with one another. What is left is only the jet yields and their corresponding luminosities. The luminosities can be grouped together and the longitudinal asymmetries can be re-written into their final form of

$$\begin{aligned} A_L &= \frac{1}{p}\frac{(N_{++}+N_{+-}) - R_L * (N_{-+}+N_{--})}{(N_{++}+N_{+-}) + R_L * (N_{-+}+N_{--})} \\ A_{LL} &= \frac{1}{p_1 * p_2}\frac{(N_{++}+N_{--}) - R_{LL} * (N_{+-}+N_{-+})}{(N_{++}+N_{--}) + R_{LL} * (N_{+-}+N_{-+})} \end{aligned} \tag{5.6}$$

Where the relative luminosities, $[R_L, R_{LL}]$, stand for $[\frac{L_{-+}+L_{--}}{L_{++}+L_{+-}}, \frac{L_{+-}+L_{-+}}{L_{++}+L_{--}}]$. The double spin case is shown in Figure 5.8. The N's are the number of jets measured by the detector for each helicity state.

The relative luminosities and the beam polarizations were not constant over the two week run. To properly account for the variations, each asymmetry is

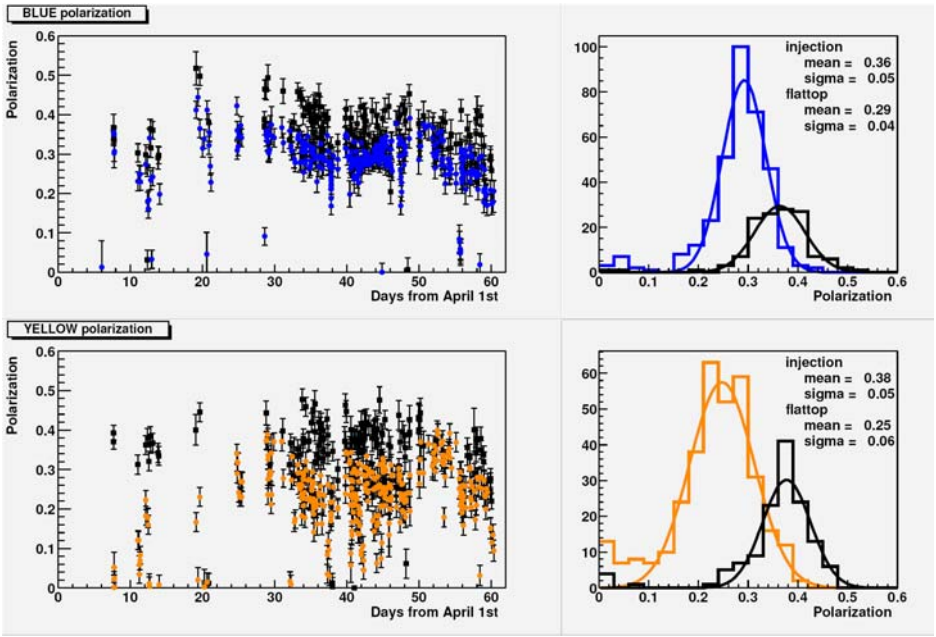

Figure 5.7: The initial polarization measurements as recorded in the RHIC ring for both proton beams. Measurements were made at injection, 23 GeV, and at flat top, 100 GeV. Measurements taken at flat top occured during data taking, however the results shown above are the initial results, not the final results.. Polarizations in a typical fills had very little degradation once ramped up to collision energy.

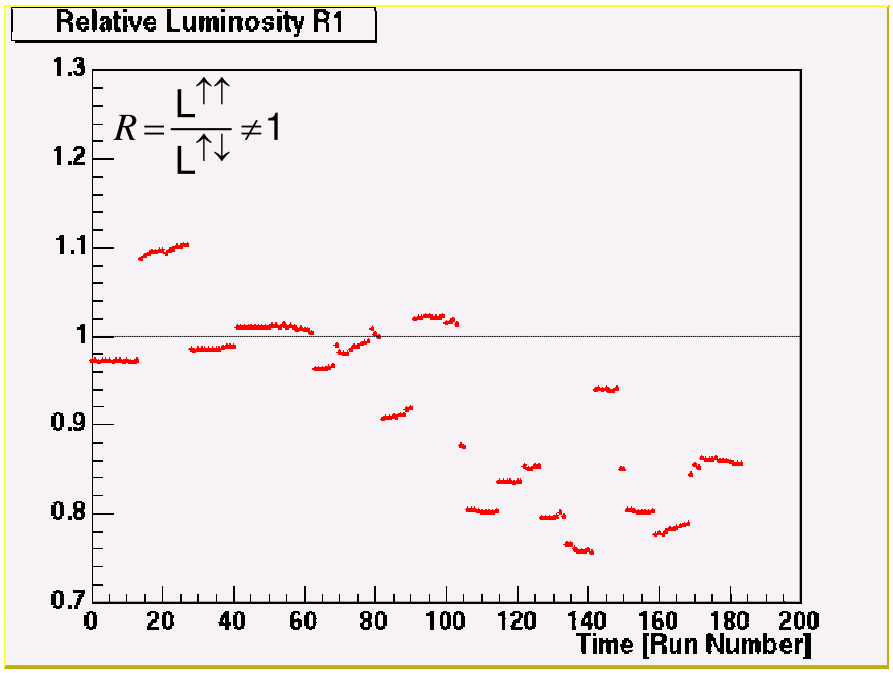

Figure 5.8: The beam bunches store varying numbers of protons, hence some bunch crossings will produce more jets than others. The relative luminosities account for this difference. The most visible characteristic of this graph is the variation fill to fill, however even within fills the relative luminosities between beams change by non-negligible amounts. The statistical and systematic errors on this ratio are on the order of 10^{-3}, roughly an order of magnitude better than the statistical uncertainty of the measurement of A_{LL}. The notation above is slightly different than notation in text, $\uparrow = -$ and $\downarrow = +$.

calculated for each run. Once all of the run-by-run asymmetries are determined, their weighted mean is found by using the standard formulas shown below.

$$\begin{aligned} \bar{x} &= \frac{\sum x_i * w_i}{\sum w_i} \\ w &= (\frac{1}{\delta(x)})^2 \\ \delta^2(x(a_j)) &= \sum (\frac{\partial x}{\partial a_j})^2 (\delta a_j)^2 \end{aligned} \tag{5.7}$$

For the single and double spin asymmetry errors, $\delta(A_L)$ and $\delta(A_{LL})$, the contributions from the polarization and relative luminosity are significantly smaller than the counting error and can be neglected. Although the polarization's uncertainty is negligible, the polarization itself substantially impacts the asymmetries errors. Single spin jets are weighted by the beam polarization squared, and jets used in the double spin asymmetry are weighted by each beam polarization squared. In practice equations 5.7 become

$$\bar{A_L} = \frac{\sum_{i}^{run} A_L^i * w_i}{\sum_{i}^{run} w_i}$$

$$\bar{A_{LL}} = \frac{\sum_{i}^{run} A_{LL}^i * w_i}{\sum_{i}^{run} w_i}$$

$$\delta A_L = \frac{1}{\sqrt{p_1^2 * N}}$$

$$\delta A_{LL} = \frac{1}{\sqrt{p_1^2 p_2^2 * N}} \tag{5.8}$$

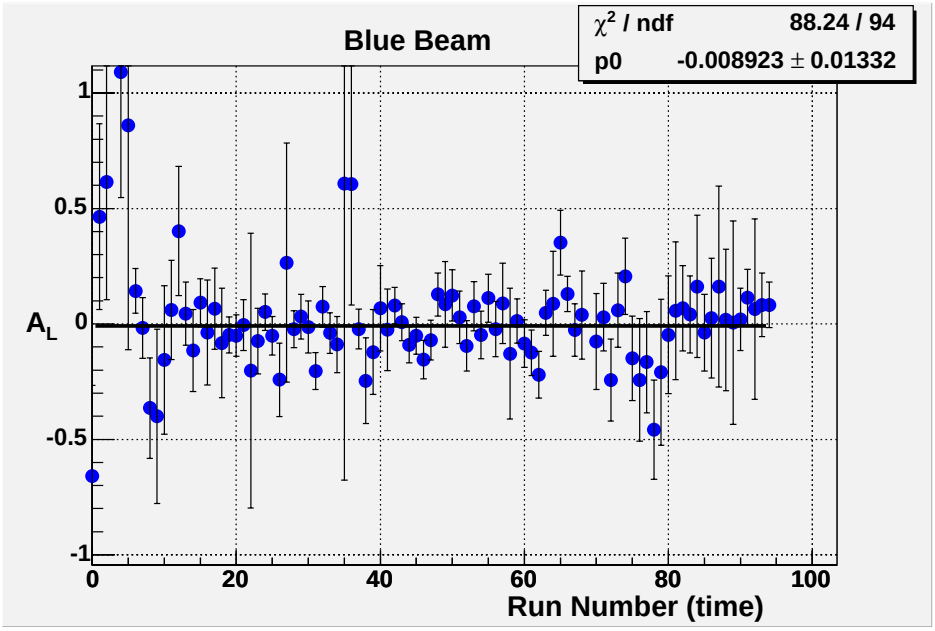

Figure 5.9: The longitudinal single spin asymmetry, A_L, of the blue beam shown as a function of time. This asymmetry is expected to be zero, and is measured to be zero to a precision of 1.5×10^{-2}.

The results from equations 5.6 and 5.8 for all three longitudinal asymmetries,

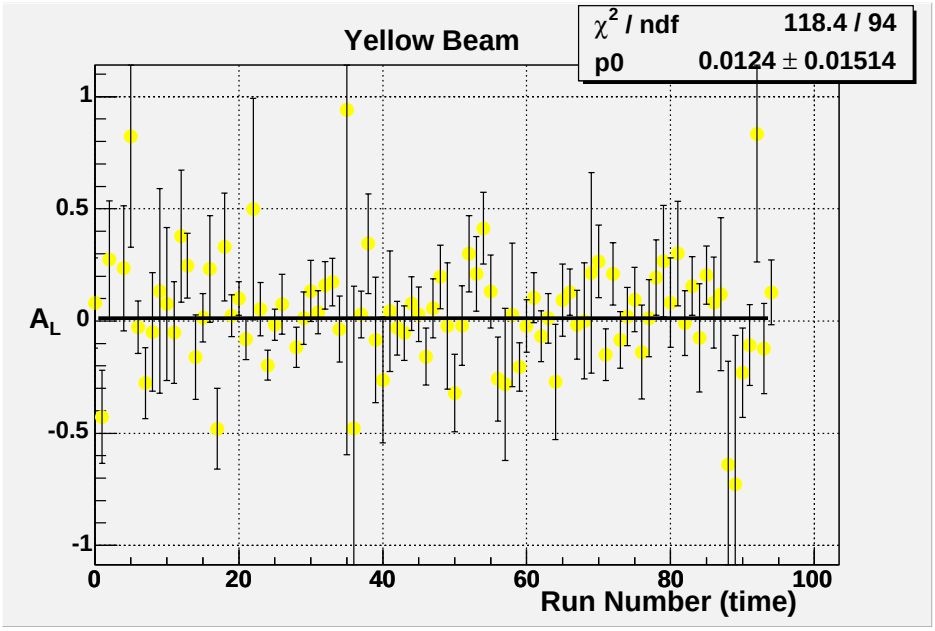

Figure 5.10: The longitudinal single spin asymmetry, A_L, of the yellow beam shown as a function of time. This asymmetry is expected to be zero and is measured to be zero to a precision of 1.5×10^{-2}.

two single spin and one double spin, are shown in Figures 5.9 through 5.11. The results from all three are statistically consistent with zero. Because the events are all weighted by the polarization in square or quadrature and the polarizations were typically between 30 and 35 percent, the statistical precision of the data is still limited, especially in the case of the double spin asymmetry, A_{LL}.

The double spin asymmetry is also examined as a function of the measured jet's $p_\perp$. A_{LL} is expected to be dependent on jet $p_\perp$ because certain sub-processes are more likely to produce jets with particular $p_\perp$'s. Recalling Figure 1.7, gluon-gluon interactions produce a greater fraction of the low $p_\perp$ jets than they do in the higher $p_\perp$ region, where the quark-quark background interactions begins to play a greater role. Calculations of A_{LL}, as seen in Figure 1.8, do predict a measurable $p_\perp$ dependence, however distinguishing between the various gluon polarizations would require a precision no worse than 10^{-2} in most bins. The

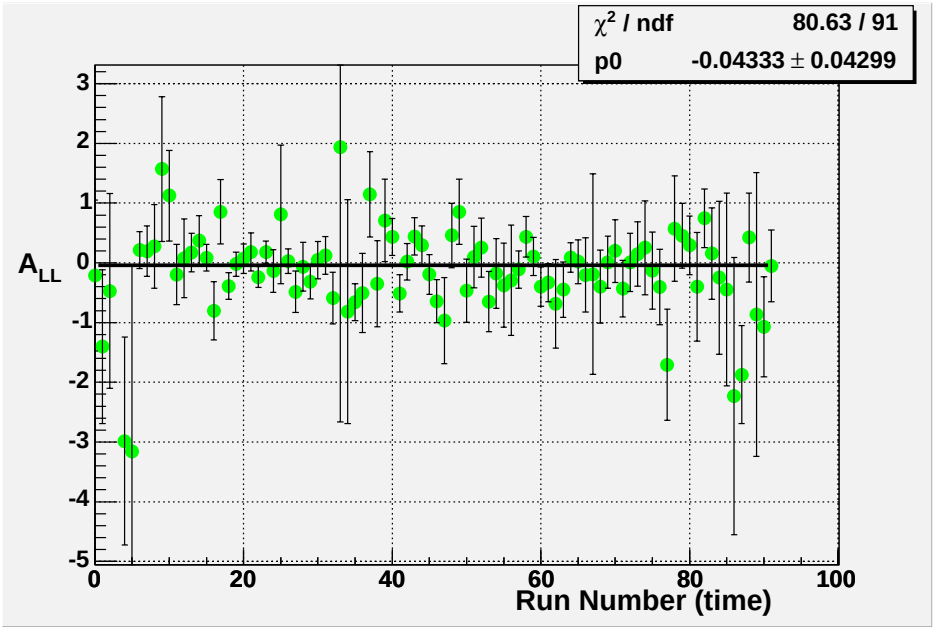

Figure 5.11: The longitudinal double spin asymmetry, A_{LL}, shown as a function of time. This asymmetry is predicted to be sensitive to the gluon's polarization. The measured asymmetry is consistent with zero to a precision of 5×10^{-2}.

2003 data as shown only provided for a bin accuracy near 10^{-1}. Understandably, no variation with $p_\perp$ is discernible in Figure 5.12.

To improve the statistical precision we can remove the cut on the software trigger threshold of 3.5 GeV of transverse energy deposited into a single tower. This cut is necessary to calculate the cross section, but removes a significant portion of the data (over half), while maintaining a very biased, but understandable sample. Although it would be difficult to understand these additional jets, their impact on the asymmetries and errors of the asymmetries is worth observing. These results are displayed in Figure 5.13. Once again, the results are consistent with zero asymmetry, however the precision of the individual bins are improved to as good as $\sim 3 \times 10^{-2}$

Any effects stemming from gluon polarization, if the gluons are indeed polar-

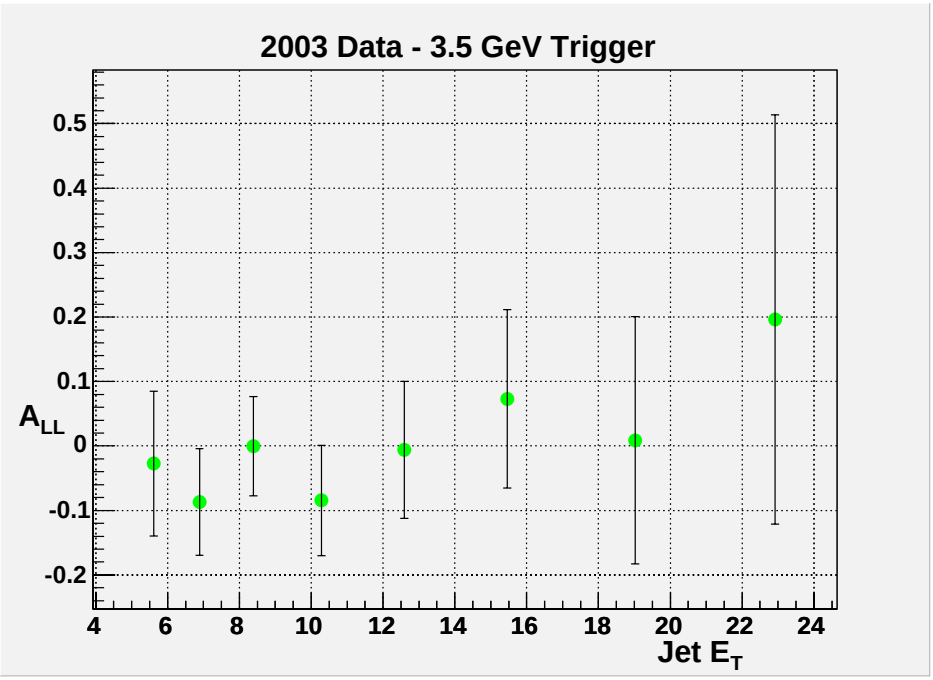

Figure 5.12: The longitudinal double spin asymmetry, A_{LL}, shown as a function of the measured jet's $p_{\perp}$. Only events containing a 3.5 GeV trigger tower are included.

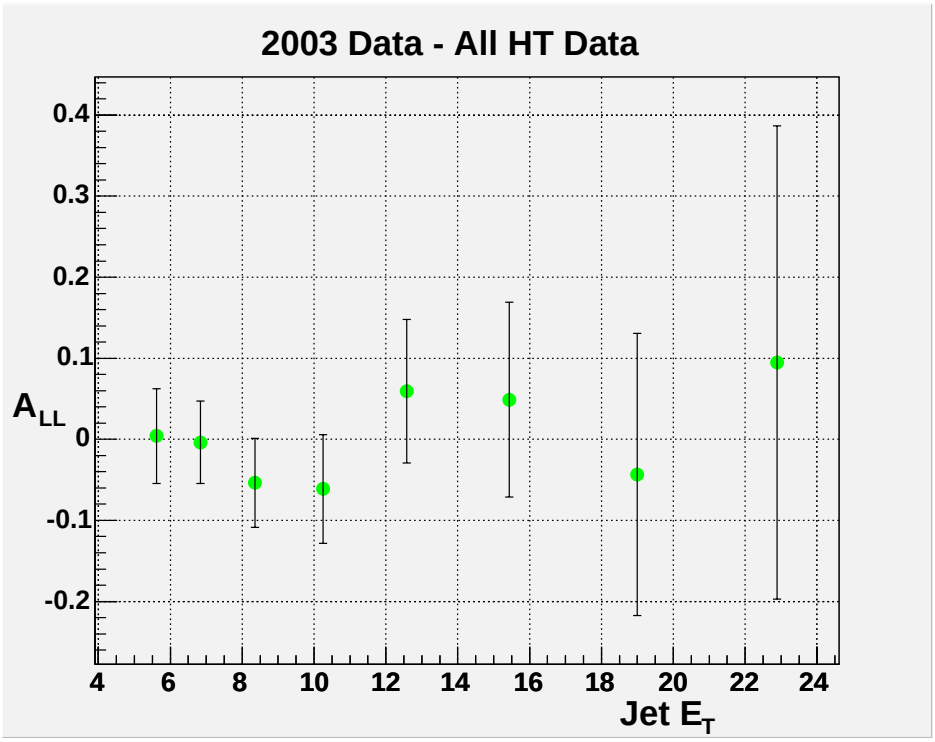

Figure 5.13: The longitudinal double spin asymmetry, $A_L L$, shown as a function of the measured jet's $p_\perp$. All high tower triggered events are counted regardless of whether or not they contain a 3.5 GeV trigger tower. The additional events improve the statistical uncertainty of the measurement, but not to a level capable of discriminating between various models of the polarized gluon structure function.

ized, are beyond the statistical precision offered in the 2003 data. Further data in upcoming years at STAR will improve upon this measurement, however the results at this time are inconclusive, yet promising.

5.2.1 A_{LL} Systematic Errors

The 2003 data for A_{LL} is limited by statistical error, however several systematic errors can also be considered. These errors will provide estimates of the precision allowable by the measurement in the coming years. From Equation 5.6 the three variables used to obtain A_{LL} are the beam polarizations, relative luminosity, and number of jets observed. If any of these quantities is poorly understanding it will reflect upon the understanding of A_{LL}.

The relative luminosities as measured by the BBC are crossed checked by a similiar detector, the zero degree calorimeter (ZDC). The ZDC is located near the beam line and functions as the minimum bias trigger for heavy ion collisions. Although it is less sensitive to proton proton collisions than the BBC, it may still serve as a useful cross check. The difference in measured relative luminosities between the two detectors was found to be zero with ± 0.003. By shifting all relative luminosities by this amount for the data the observed A_{LL} shifts by 1.3% for each bin.

The beam polarizations factor into both A_{LL} and $\delta(A_{LL})$ identically. Therefore any systematic shift to the polarizations true value uniformly scales with the asymmetry and its error. From the results of the jet target experiment performed in 2004, the beam polarization is known to better than 10%. Once again shifting the polarizations within the analysis results in a systematic uncertainty of $\pm 0.3\%$.

The final consideration is contamination from beam background. As shown in section 5.1.3, the jets caused by beam background can be estimated to be $7.5 \pm 2\%$

of the total number of measured jets after cuts to remove the background are placed on the data. The asymmetry analysis is then repeated using a reverse cut to select only on background jets within the measurement region. The asymmetry of these jets is found to be -0.006 ± 0.024. If the asymmetry is indeed zero then the backgound may still dilute the asymmetry measurement. The second possibility is that the 7.5% of the background jets have an asymmetry as large as 0.026 ± 0.006. Niether of these effects is larger than 0.3%.

The systematic errors presented in the inclusive jet cross section are not applicable to the asymmetry measurement. Any error to the cross section will factor out of the asymmetry's numerator and denominator and cancel.

Run	MB $\|z\| < 75$	Pre-scale	Normalization	Total MB Events
4137012	5707	2600	1.123	1.66633e+07
4137013	4369	2600	1.123	1.27566e+07
4137015	3094	2600	1.123	9.03386e+06
4137017	3062	2500	1.123	8.59656e+06
4137018	519	2500	1.123	1.45709e+06
4137030	11489	3800	1.123	4.90282e+07
4137032	7394	3250	1.123	2.69863e+07
4137035	3603	2600	1.123	1.052e+07
4137036	820	2540	1.123	2.33898e+06
4137037	1416	2480	1.123	3.94362e+06
4142004	997	2900	1.123	3.24693e+06
4142005	1598	2600	1.123	4.66584e+06
4142006	3605	2500	1.123	1.0121e+07
4142008	2113	2200	1.123	5.22038e+06
4142010	2261	2000	1.123	5.07821e+06
4142011	11243	1800	1.123	2.27266e+07
4142012	8638	1500	1.123	1.45507e+07
4142018	14261	2200	1.123	3.52332e+07
4142029	3174	1820	1.123	6.48721e+06
4143003	5584	2200	1.123	1.37958e+07
4143006	2987	2000	1.123	6.7088e+06
4143013	1850	1600	1.123	3.32408e+06
4143027	17818	3400	1.123	6.80327e+07
4144004	5838	9100	1.123	5.96603e+07
4144005	4559	8200	1.123	4.1982e+07
4144006	259	7400	1.123	2.15234e+06
4144017	3543	6100	1.123	2.42706e+07
4144018	3019	6000	1.123	2.0342e+07
4144019	13031	5500	1.123	8.0486e+07
4144022	14831	4800	1.123	7.9945e+07
4144023	247	4300	1.123	1.19274e+06

Table 5.1: Number of total minimum bias events between within 75 cm of STAR's center that occured during the 2003 data taking. An overall normalization correction of 1.123 accounts for the events that did not have their collision points reconstructed by the TPC. The total number of events, last column, is the multiplicative product of the three center columns.

Run	MB $\|z\| < 75$	Pre-scale	Normalization	Total MB Events
4144025	4156	4200	1.123	1.96022e+07
4144026	398	4000	1.123	1.78782e+06
4144039	8787	6450	1.123	6.36473e+07
4145010	3399	6000	1.123	2.29025e+07
4145023	4985	5500	1.123	3.07899e+07
4145024	5056	5500	1.123	3.12284e+07
4145037	8912	6900	1.123	6.90564e+07
4145038	7042	6250	1.123	4.9426e+07
4145040	371	5900	1.123	2.45813e+06
4145041	15320	5800	1.123	9.97853e+07
4145042	14036	5300	1.123	8.35409e+07
4145043	15246	4800	1.123	8.2182e+07
4145044	9511	4400	1.123	4.69958e+07
4146002	465	4200	1.123	2.19322e+06
4146003	19559	4200	1.123	9.2252e+07
4146005	4904	3700	1.123	2.03766e+07
4147002	1862	7000	1.123	1.46372e+07
4147003	1894	6800	1.123	1.44633e+07
4147004	448	6800	1.123	3.42111e+06
4147006	2305	6400	1.123	1.65665e+07
4147007	10743	6300	1.123	7.60057e+07
4147009	12117	5800	1.123	7.89229e+07
4147010	1336	5000	1.123	7.50164e+06
4147011	14052	4900	1.123	7.73239e+07
4147012	13579	4600	1.123	7.01464e+07
4147013	15209	4200	1.123	7.17348e+07
4147014	15131	3800	1.123	6.457e+07
4147015	14603	3500	1.123	5.73971e+07
4147016	3665	3200	1.123	1.31705e+07
4147029	1092	9000	1.123	1.10368e+07
4147030	4905	8800	1.123	4.84732e+07

Table 5.2: Number of total minimum bias events between within 75 cm of STAR's center that occured during the 2003 data taking. An overall normalization correction of 1.123 accounts for the events that did not have their collision points reconstructed by the TPC. The total number of events, last column, is the multiplicative product of the three center columns.

Run	MB $\|z\| < 75$	Pre-scale	Normalization	Total MB Events
4147031	5260	8400	1.123	4.96186e+07
4147032	5679	8000	1.123	5.10201e+07
4147033	7009	7600	1.123	5.98204e+07
4147034	7304	7300	1.123	5.98775e+07
4147036	8244	6600	1.123	6.11029e+07
4147037	6902	6200	1.123	4.80559e+07
4147050	1192	4800	1.123	6.42536e+06
4147051	1861	4600	1.123	9.61355e+06
4148006	1679	2	1.123	3771.03
4148007	14676	2	1.123	32962.3
4148011	14761	2	1.123	33153.2
4148012	18433	2	1.123	41400.5
4148013	19000	2	1.123	42674
4148014	20758	2	1.123	46622.5
4148015	101478	1	1.123	113960
4148016	11183	1	1.123	12558.5
4148025	258	3	1.123	869.202
4148026	8388	2	1.123	18839.4
4148027	16355	4300	1.123	7.89767e+07
4148029	9003	3500	1.123	3.53863e+07
4148032	3348	3200	1.123	1.20314e+07
4148044	1898	7700	1.123	1.64122e+07
4148045	445	7200	1.123	3.59809e+06
4148046	3568	7100	1.123	2.84487e+07
4148048	8155	6800	1.123	6.22748e+07
4149001	5989	6550	1.123	4.4053e+07
4149004	237	6000	1.123	1.59691e+06
4149005	8820	5700	1.123	5.64577e+07
4149006	9137	5300	1.123	5.43825e+07
4149007	9393	5000	1.123	5.27417e+07
4149008	3367	4730	1.123	1.78848e+07

Table 5.3: Number of total minimum bias events between within 75 cm of STAR's center that occured during the 2003 data taking. An overall normalization correction of 1.123 accounts for the events that did not have their collision points reconstructed by the TPC. The total number of events, last column, is the multiplicative product of the three center columns.

Run	MB $\|z\| < 75$	Pre-scale	Normalization	Total MB Events
4149009	5682	4550	1.123	2.9033e+07
4149010	5763	4360	1.123	2.82173e+07
4149012	2975	4230	1.123	1.41321e+07
4149013	4563	3800	1.123	1.94721e+07
4149014	3378	3700	1.123	1.40359e+07
4149015	1196	3550	1.123	4.76803e+06
4149016	9955	3400	1.123	3.80102e+07
4149018	13321	3500	1.123	5.23582e+07
4149019	4241	3300	1.123	1.57167e+07
4149020	13951	3200	1.123	5.01343e+07
4149021	5622	2961	1.123	1.86943e+07
4149022	14814	2801	1.123	4.65978e+07
4149024	2892	2617	1.123	8.49927e+06
4149059	2219	2800	1.123	6.97742e+06
4149060	2576	5000	1.123	1.44642e+07
4149063	1701	3300	1.123	6.30374e+06
4150004	9494	8000	1.123	8.52941e+07
4150005	13376	7200	1.123	1.08153e+08
4150008	1650	6000	1.123	1.11177e+07
4150009	16085	6000	1.123	1.08381e+08
4150010	34363	5300	1.123	2.04525e+08

Table 5.4: Number of total minimum bias events between within 75 cm of STAR's center that occured during the 2003 data taking. An overall normalization correction of 1.123 accounts for the events that did not have their collision points reconstructed by the TPC. The total number of events, last column, is the multiplicative product of the three center columns.

$p_\perp$ Bins	Average $p_\perp$	σ [mbarns/GeV^2]	Statistical Error
5 - 6	5.53	0.000510084	0.000359955
6 - 7	6.47	0.00030541	0.000175529
7 - 8	7.47	0.000136128	7.77873e-05
8 - 9	8.47	7.9654e-05	5.5567e-05
9 - 10	9.47	4.96191e-05	4.88238e-06
10 - 11	10.47	2.62398e-05	2.86373e-06
11 - 12	11.48	1.11473e-05	1.24793e-06
12 - 13	12.46	7.25013e-06	9.50335e-07
13 - 14	13.47	2.47075e-06	3.04069e-07
14 - 15	14.47	3.09621e-06	5.83481e-07
15 - 16	15.47	1.17428e-06	1.87177e-07
16 - 17	16.48	7.30906e-07	1.34914e-07
17 - 18	17.49	4.04553e-07	7.41324e-08
18 - 19	18.47	3.65388e-07	7.97533e-08
19 - 21	19.93	2.41535e-07	1.1174e-08
21 - 25	22.68	6.95586e-08	3.08033e-09
25 - 29	26.78	1.54603e-08	1.05064e-09
29 - 33	30.78	3.88165e-09	4.38465e-10
33 - 37	34.77	1.36841e-09	2.05194e-10
37 - 41	37.98	5.89132e-10	1.23811e-10

Table 5.5: Inclusive differential cross section of jets measured by STAR in 2003.

Fill	Blue Polarization	Yellow Polarization
3732	16.4	30.9
3733	38.8	31.0
3757	46.5	41.8
3759	48.0	46.2
3764	46.3	44.2
3765	42.8	35.0
3769	39.0	44.6
3770	45.1	38.7
3780	34.6	27.9
3793	40.4	25.7
3796	33.7	22.6
3797	50.6	27.7
3799	35.0	33.2
3801	41.9	33.2
3803	26.1	32.6
3809	27.9	18.2
3810	23.6	15.7

Table 5.6: The polarizations from the blue and yellow beams as determined by the CNI polarimeter group. These values include the offline CNI data when applicable and the CNI scaler data (normalized by 1.09 and 1.05 for Blue and Yellow) when offline data was not available. Normalizations from the jet target results to the CNI data of 1.23 and 1.21 applied to the Blue and Yellow beams are included in this table. These polarization values are used in the analysis.

Jet $p_\perp$ Bins	Average Jet $p_\perp$ in Bin	A_{LL}	$\delta(A_{LL})$
5 - 6.15	5.64838	-0.028	0.11
6.15 - 7.56	6.88814	-0.087	0.08
7.56 - 9.30	8.39176	-0.000	0.08
9.3 - 11.44	10.2811	-0.085	0.09
11.44 - 14.08	12.5899	-0.006	0.11
14.08 - 17.3	15.4609	0.073	0.14
17.3 - 21.3	19.023	0.009	0.19
21.3 - 25	22.915	0.196	0.32
5-25	9.185	-0.0296	0.0375

Table 5.7: A_{LL} results taken from Figure 5.12.

Jet $p_\perp$ Bins	Average Jet $p_\perp$ in Bin	A_{LL}	$\delta(A_{LL})$
5 - 6.15	5.62743	0.00306926	0.058592
6.15 - 7.5645	6.83444	-0.00364215	0.050916
7.5645 - 9.30434	8.35701	-0.0536245	0.0548057
9.30434 - 11.443	10.2557	-0.061298	0.0671066
11.443 - 14.0765	12.5773	0.0593867	0.0884622
14.0765 - 17.3141	15.4366	0.0488657	0.120196
17.3141 - 21.2964	18.9919	-0.0433509	0.173865
21.2964 - 25	22.8864	0.0948574	0.291834
5-25	8.046	-0.0144689	0.0260481

Table 5.8: A_{LL} results taken from Figure 5.13.

CHAPTER 6

Discussion

6.1 Summary

RHIC has begun a program to study the inner workings of the nucleon by providing high energy collisions of polarized protons with polarized protons. Longitudinally polarized proton-proton collisions provide several opportunities to expand the current knowledge base that has been accumulated by the deep inesastic scattering community over the past thirty to forty years. The first scheduled addition to his knowledge base is the better understandment of the gluon's polarization within the nucleon. Hopefully this will answer the question first posed in 1987 by the European Muon Collaboration, when after measuring the quark's contribution to the proton's angular momentum realized that it fell short of the complete sum.

Several interesting measurements deriving from gluon interactions can be measured at mid-rapidity in an effort to understand the gluon's polarization. Many of the possible measurements are of exclusive processes, such as $g + g- > photon + photon$, $g + q- > photon + jet$, $g + g- > (pairofheavyquarks)$, etc. Exclusive channels are particularly attractive because they are clean and may be clearly predicted by theory. However from an experimental perspective, they are the least accessible and most statistically limited. A more accessible quantity at STAR is an inclusive measrument of jets falling within the the accecptance region

of 0 to 1 in η. Although an inclusive measrument is more convoluted, including non-gluon contributions from quark-quark scattering, a discernable signal should propogate from the quark-gluon and gluon-gluon contributions. This thesis is STAR's first effort to measure the inlcusive jet channel.

To aid STAR's endevor, the first half of the barrel EMC was installed in 2003. The BEMC provides a substantial contribution to STAR's detection capabilities in the mid rapidity region. Coupled with the tracking of charged tracks by the TPC, the bulk of particles produced at $0 < \eta < 1$ may be measured and used in jet reconstruction. Secondly as a fast detector, the energy measurements made by the BEMC towers can also be integrated into the triggering system. This allowed us to select the most energetic events which are substantially more likely to occur from the hard scatterings processes of quark-quark, quark-gluon and gluon-gluon. Because we are limited in the volume of data STAR can read out, selecting events most relevent to the analysis is a key concern.

In Chapters 4 and 5 the data from the 2003 proton-proton run was presented. The 2003 run lasted for two weeks, and in that time STAR sampled ~ 330 inverse nanobarns of collisions and recorded the most energetic events from ~ 170 inverse nanobarns. The two principle results from the inclusive jet analysis are show in Chapter 5, the inclusive jet cross section and the asymmetry of the spin-dependent cross sections, A_{LL}.

The inclusive jet cross sections for jets with an η-ϕ radius of 0.4 (Figure 5.4) matches well with NLO pQCD calculations (Figure 5.5). The data points are corrected by using the simulation packages Pythia and Geant. Because of the trigger inefficiency, large corrections are necessary particularly in the low transverse energy region. Addition investigation and progress on these results is underway, however these early results indicate that the path we are on is indeed

the correct one.

The three longitudinal asymmetries (A_L^{blue},A_L^{yellow},A_{LL}) are all shown to be consistent with zero to within the statistical precision of 2003. The single spin asymmetry is expected to be zero, making it a useful null-result to check. The double spin asymmetry, A_{LL}, is expected to deviate from zero depending upon the gluon's polarization. However the deviation from zero is expected to be small, and any deviation which may exist was beyond the statistical reach provided by the 2003 sample.

6.2 The Future

The spin program at RHIC is dedicated to pursuing a detailed understanding of the gluon's polarization in the upcoming years. Several improvements made to both STAR and RHIC are underway, many of which are complete at the point of this writing.

Beginning with STAR, the most notable additions will be the full installation of electromagnet calorimetry. The half barrel EMC will be competed, doubling its coverage from $0 < \eta < 1$ to $-1 < \eta < 1$. Additionally an endcap EMC, covering the region from $1 < \eta < 2$ is now installed and operational as of 2004. The additional coverage area provided by the fully-installed calorimetry both increases the number of inclusive jets measurbale and provides the area necessary to make di-jet and photon+jet measurements.

A second addition to STAR, which was not initially expected, is now underway. Data from 2003 detected a substantial source of background particles originating from an upstream beam source. Schematics are yet to be finalized, however plans exist to install a large shielding between the magnets used to steer

and focus the proton beam and the STAR interaction area. A large buffer of iron or concrete placed in this region would greatly reduce traversing beam which has been misdirected by the magnet(s).

RHIC upgrades come in two forms. The first is larger luminosities, i.e. more collisions, and a greater chance to record rarer events on a minute to minute basis. Because of the costs associated with running a large facility such as RHIC, the benefits of increased beam intensities are substantial.

The second and arguably more substantial improvement will take place on the beam's polarization. In 2003 the beam polarization was near 30% throughout the running period. This number increased to 35% in 2004, and to 45-50% in 2005 (official numbers for 2005 are not yet available). The target luminosity of 70% is expected to be achieved during the 2006 or 2007 running periods. Because each event is weighted by the beam polarization, either by the square in the case of A_L or in quadrature in the case of A_{LL}, a high polarization significantly effects the statistical merit of the asymmetry measurements.

Work is also underway to study 500 GeV proton-proton collisions. The higher energy collisions probe an separate kinematic space, thereby providing a greater lever arm toward the understanding of the gluon polarization. Additionally we may begin to discern the anti-quark contribution to the proton's angular momentum from the quark contribution. Previous experiments, though able to determine the total quark/anti-quark contribution, where not able to make this separation. The measurement will be made by examining forward W production, which is predicted to be sensitive to the up, anti-up, down, and anti-down quark's polarizations. In order to successfully reconstruct the W from the high momentum electron-position pairs addition forward tracking at STAR will be required. Plans to build this tracker are well underway at STAR.

Finally, RHIC is now committing to longer polarized proton-proton runs. In 2003 data from longitudinally polarized proton-proton collisions was gathered over a two week period. In 2005 data was recorded for nearer 2 months, and this number will be doubled again during the 2006 running period.

References

[Ada03] J. Adams et al. " Transverse Momentum and Collision Energy Dependence of High p(T) Hadron Suppression in Au+Au Collisions at Ultrarelativistic Energies " *Phys. Rev.*, **D58**:1112002, 1998.

[Ade98] B. Adeva et al. *Phys. Rev.*, **D58**:1112002, 1998.

[Aid05] C. Aidala et al. "Research Plan for Spin Physics at RHIC" 2005.

[Ash88] J. Ashman et al. *Phys. Rev.*, **B206**:364, 1988.

[Bou03] C. Bourrely and J. Soffer "Do we understand the single spin asymmetry for pi0 inclusive production in pp collisions?" *Eur. Phys. J.*, **C36**:371, 2004.

[Est33] I. Estermann, R. Fricsh, O. Stern "" *Nature*, **132**:169, 1933.

[Geh96] T. Gehrmann and W. J. Stirling *Phys. Rev.*, **D53**:6100, 1996.

[Har03] J. Harai and S. Kumano and N. Saito "Determination of polarized parton distribution functions and their uncertainties" *Phys. Rev.*, **D69**:054021, 2004.

[Lea03] E. Leader and A. Sidorov and D. Stamenov "Importance of Higher Twist Corrections in Polarized DIS" *DIS2003 Workshop*, :, 2003.

[PDG] S. Eidelman et al. *Phys. Lett.*,**B529**:1, 2004. "http://durpdg.dur.ac.uk/lbl/"

[Sjo] T. Sjostrand "http://www.thep.lu.se/ torbjorn/Pythia.html"

[Sua1] A. Suaide "http://www.star.bnl.gov/protected/highpt/suaide/calib2003/ElectronCalib/"

[Sua2] A. Suaide "http://www.star.bnl.gov/protected/highpt/suaide/calib2003/MIP/"